Structural and Biochemical Studies on selected Chlorite Dismutases

MASTER THESIS

submitted by

Michael Krutzler, BSc.

in November 2017

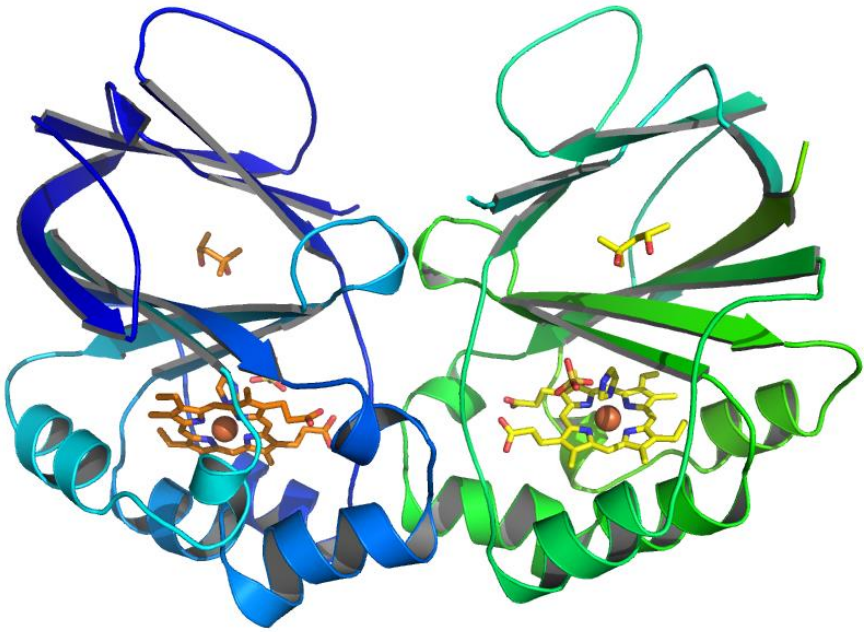

Department of Chemistry - Division of Biochemistry - Protein Biochemistry Group

BOKU - University of Natural Resources and Life Sciences

Muthgasse 18, 1190 Vienna, Austria

“We cannot see our reflection in running water.

It is only in still water that we can see.”

Zen saying

ICH DANKE

CHRISTIAN OBINGER, PAUL GEORG FURTMÜLLER UND KRISTINA DJINOVIĆ-CARUGO

IRENE SCHAFFNER, STEFAN HOFBAUER UND GEORG MLYNEK

ANNEMARIE NEUGEBAUER, EDUARD DOMSCHITZ UND THERESA KRUTZLER.

BESONDERER DANK AN SUSANNE SPATH.

Abstract

Chlorite is a toxic substance that is typically used as an agent in the bleaching industry but is also a necessary component in rocket fuels. Its accumulation in ground and surface waters raised concern in recent years and it is of increasing interest to find remediation strategies to deal with this problem. The metalloenzyme chlorite dismutase (Cld) may serve this purpose in the future. It contains heme *b* and uses chlorite as substrate in the following catalyzed reaction: $ClO_2^- \rightarrow Cl^- + O_2$. Thus, it not only detoxifies chlorite by converting it into harmless chloride, but also produces one molecule of dioxygen. The formation of a covalent oxygen-oxygen bond is rather uncommon and only performed by oxygenic organisms during photosynthesis and by an anaerobic methane-oxidizing bacterium. Originally discovered in perchlorate reducing bacteria (PCRB), the chlorite dismutase family meanwhile comprises many members, a lot of them not capable of metabolizing perchlorate. While in PCRB their function is the detoxification of chlorite which is the resulting species upon reduction of perchlorate and chlorate, the physiological role of Cld in non-PCRB is not clear. Those functional Clds are structurally related to HemQs (also called non-functional Clds) and dye-decolorizing peroxidases, both sharing the same fold but conducting different biochemical reactions. Three proteins are examined in this thesis: Cld of "*Candidatus* Nitrospira defluvii" (NdCld) as representative of clade 1 of functional Clds, Cld of *Cyanothece* sp. PCC7425 (CCld) as representative of clade 2 of functional Clds and HemQ of *Listeria monocytogenes* (LmCld) as representative of non-functional Clds. The goal was a biochemical, biophysical and structural characterization with emphasis on a comparison of the proteins under study. This was achieved using a set of different biochemical methods and a crystallographic approach.

Zusammenfassung

Chlorit ist eine anthropogene und giftige Substanz. Sie ist ein wichtiges Agens in der Bleichindustrie aber auch eine notwendige Komponente in Raketentreibstoffen. In letzter Zeit kamen durch die zunehmende Akkumulierung in Grundwasser und Oberflächengewässern Bedenken auf und seitdem besteht ein zunehmendes Interesse sich dieses Problems anzunehmen. Das Metalloenzym Chlorit Dismutase (Cld) könnte dieser Aufgabe zukünftig gerecht werden. Es beinhaltet Häm b und nutzt Chlorit als Substrat in der folgenden katalysierten chemischen Reaktion: $ClO_2^- \rightarrow Cl^- + O_2$. Zusammengefasst entgiftet es also nicht nur Chlorit durch die Umwandlung in harmloses Chlorid, sondern produziert auch ein Molekül Disauerstoff. Die Bildung einer kovalenten Sauerstoff-Sauerstoff Bindung ist ungewöhnlich und wird nur von oxygenen Organismen während der Photosynthese, aber auch von einem anaeroben, Methan-oxidierenden Bakterium ausgeführt. Nachdem Chlorit Dismutasen in Perchlorat reduzierenden Bakterien entdeckt wurden stellen sie mittlerweile eine Familie mit zahlreichen Mitgliedern dar von denen mehrere Vertreter Perchlorat nicht abbauen können. Während die Funktion von Chlorit Dismutasen in Perchlorat reduzierenden Bakterien darin besteht Chlorit, welche die resultierende Spezies der Reduktion von Perchlorat darstellt, zu entgiften, ist es noch nicht eindeutig geklärt welche physiologische Rolle sie in anderen Bakterien ausüben. Diese sogenannten funktionalen Chlorit Dismutasen sind strukturell verwandt mit HemQs (oder auch dysfunktionale Chlorit Dismutasen) und Dyp-type Peroxidasen, katalysieren jedoch unterschiedliche chemische Reaktionen. In dieser Arbeit werden drei Clds genauer untersucht: Cld von "*Candidatus* Nitrospira defluvii" (NdCld) als Vertreter von Klade 1, Cld von *Cyanothece* sp. PCC7425 (CCld) als Vertreter von Klade 2 (beide Kladen stellen einen Teil der funktionalen Clds dar) und Cld von *Listeria monocytogenes* als Vertreter von nicht-funktionalen Clds. Das Ziel war es eine biochemische, biophysikalische und strukturelle Charakterisierung aller erwähnten Clds, aber auch einen Vergleich der untersuchten Proteine untereinander durchzuführen. Mit Hilfe eine Reihe von biochemischen Methoden, aber auch eines röntgenkristallographischen Ansatzes konnte dieses Ziel erreicht werden.

Table of contents

1 Introduction

Chlorite dismutases (Clds) are heme *b* containing enzymes which catalyze the following reaction:

$$ClO_2^- \rightarrow Cl^- + O_2$$

They were originally discovered in perchlorate-reducing bacteria which utilize perchlorate and chlorate as terminal electron acceptors in the absence of oxygen and produce chlorite as an intermediate in their respiratory chain [1,2]. Since chlorite is a strong oxidant, it would harm the cell if not reduced to non-toxic Cl^- by chlorite dismutase. Moreover, a covalent oxygen-oxygen bond is formed during turnover which is rather uncommon and only catalyzed by the water-splitting manganese complex of photosystem II of oxygenic organisms, and an enzyme of an anaerobic methane-oxidizing bacterium [3]. Chlorite itself is an anthropogenic substance, which can be found in bleaching agents or rocket fuels. The heavy usage leads to an accumulation in ground water, surface waters and soils [4]. Because of this, chlorite dismutases are of high interest, potentially providing an interesting mechanism to deal with these problems in the future.

1.1 Phylogeny

The *cld* gene is widely distributed across bacteria and archaea (see Figure 1.1). It can be distinguished between functional Clds which show chlorite decomposition activity and non-functional Clds which lack the distal arginine residue and cannot degrade chlorite into chloride and dioxygen. Little is known about the physiological role of the latter, but there is also an ongoing debate about the proper substrate of the former, since e.g. *Cyanobacteria* and *Nitrospirae* possess functional Clds but do not produce chlorite intracellularly. Moreover, Clds and so-called dye-decolorizing peroxidases (DyP) can be rooted against each other, which suggests a common ancestor for those structurally but not functionally related proteins. Functional Clds can be further divided into two lineages, differing basically in sequence length, oligomeric composition and stability: There are the "long Clds" (clade 1) and the "short Clds" (clade 2), the former being characterized in more detail [5].

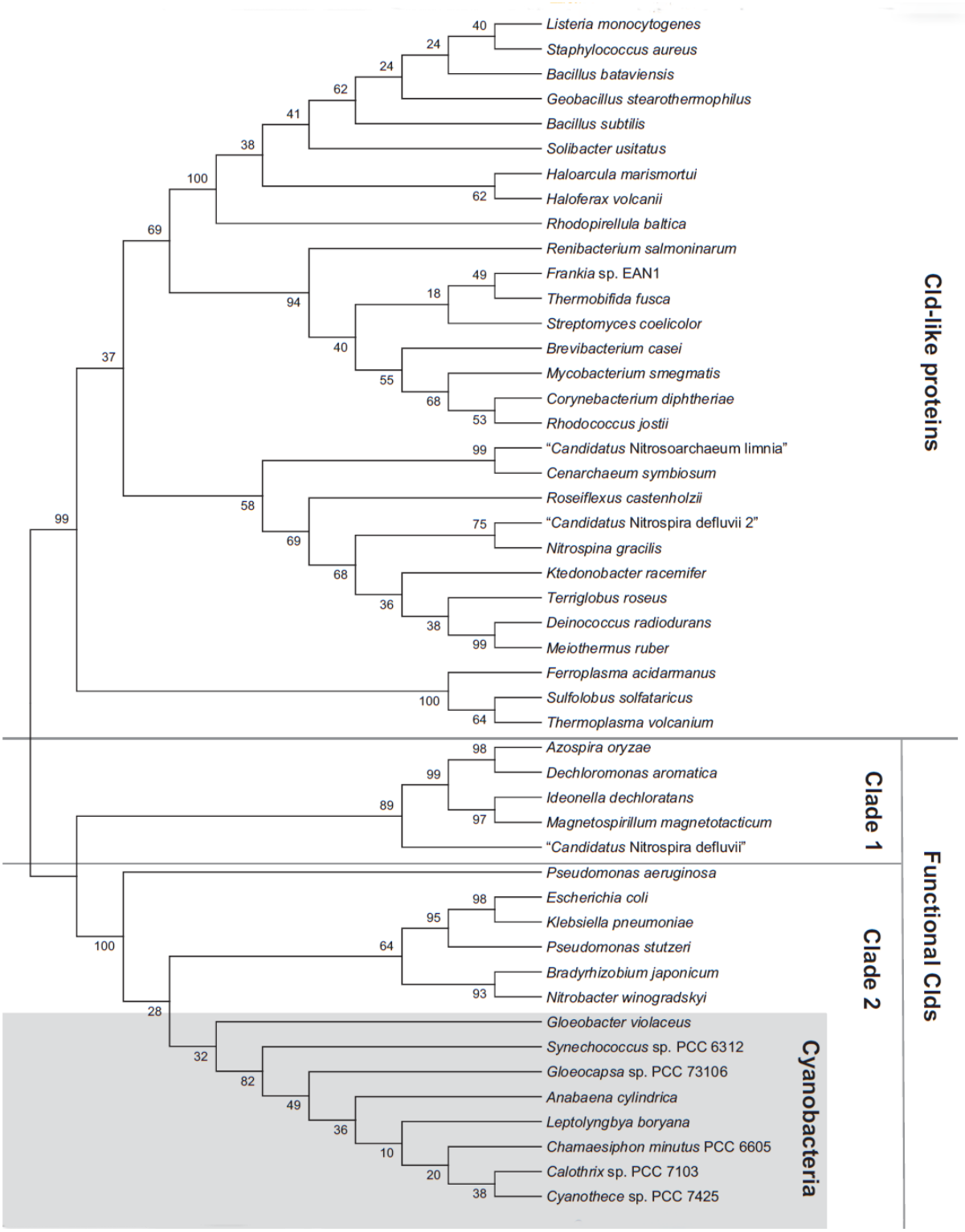

Figure 1.1: Reconstructed phylogenetic tree of Cld-like and functional Cld protein sequences [6].

1.2 Architecture of heme *b*

Heme is a cofactor which consists of a porphyrin ring with an iron atom in the center. Porphyrin is a heterocyclic ring which is made up of four pyrrolic groups joined by methine bridges. Additionally, the porphyrin of heme *b* (also known as protoheme IX or protoporphyrin IX) has 4 methyl, two vinyl and two propionate substituents. Many important proteins, such as hemoglobin, myoglobin, cytochrome and catalase contain heme as redox cofactor. For example, hemoglobin serves as oxygen-transporting metalloprotein in the red blood cells of all vertebrates.

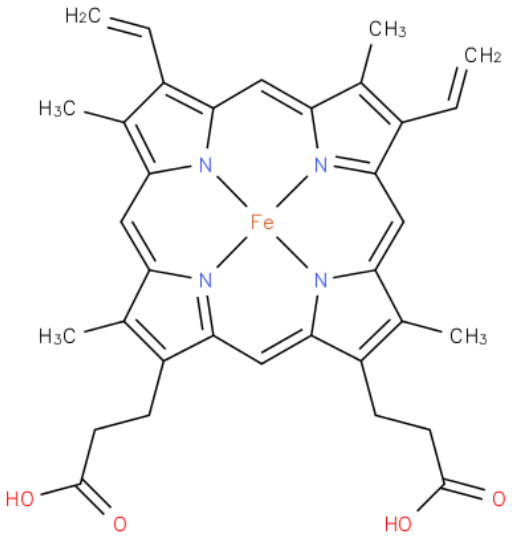

Figure 1.2: Architecture of heme *b* [7].

1.3 Spin states

In Clds, iron naturally occurs in its ferric oxidation state Fe(III). In the course of the structural studies which are performed with CCld in this thesis using X-ray crystallography, a beam of incoming X-rays reduces ferric Fe(III) to ferrous Fe(II). Both oxidation states may exist in two different spin states (see chapter 1.3.1 and 1.3.2) whose formation highly depends on the distal ligand. The change in spectral properties can be investigated using UV-vis spectroscopy.

1.3.1 Ferrous iron Fe(II)

Ferrous iron may exist in two possible states assuming an octahedral configuration. This depends on the strength of the respective ligand field. In its high-spin state (S=2), the six valence electrons are distributed along the five d-orbitals according to Hund's rule (see Figure 1.3), which results in four unpaired electrons. In the low-spin state (S=0), the difference of energy levels between the d-orbitals is

larger which makes the occupation of higher level d-orbitals energetically unfavourable. This results in no unpaired electrons.

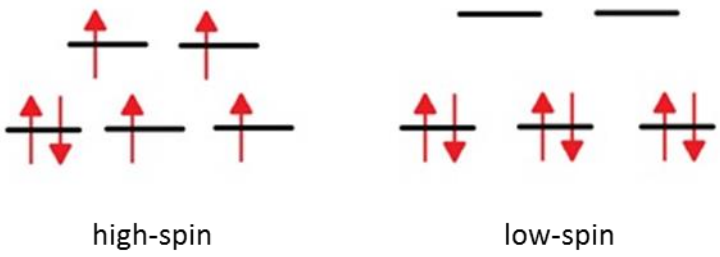

Figure 1.3: Spin states of ferrous Fe in octahedral configuration. Black horizontal lines represent the 5 d-orbitals while the red arrows represent valence electrons. Arrows pointing in opposite directions represent electrons with opposite spin.

1.3.2 Ferric iron Fe(III)

The theory mentioned above also applies for ferric iron assuming an octahedral configuration. In its high-spin state (S= 5/2) the 5 valence electrons are distributed along the 5 d-orbitals which results in five unpaired electrons (see Figure 1.4). The low-spin state (S=1/2) has one unpaired electron.

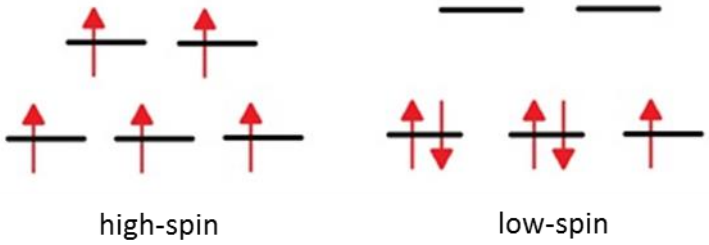

Figure 1.4: Spin states of ferric Fe in octahedral configuration. Black horizontal lines represent the 5 d-orbitals while the red arrows represent valence electrons. Arrows pointing in opposite directions represent electrons with opposite spin.

1.4 Subunit structure and active site architecture of studied chlorite dismutases

Three different proteins of the chlorite dismutase family are presented in this thesis:

- Cld of "*Candidatus* Nitrospira defluvii" (NdCld) and its two mutants K141E and E210A as representatives of clade 1 (functional Clds).
- Cld of *Listeria monocytogenes* (LmCld) as representative of Cld-like proteins (non-functional Clds, HemQ).
- Cld of *Cyanothece* sp. PCC7425 (CCld) as representative of clade 2 (functional Clds).

1.4.1 NdCld

NdCld was found to be a pentameric protein in solution and in its crystallized state [8]. Each subunit has two domains, each consisting of four antiparallel β-sheets. It is flanked on both sides by six α-helices and resembles the topology known as ferredoxin-like fold. In each domain, two α-helices run parallel to each β-sheet and two shorter ones run perpendicular to the latter, forming a cavity which is larger in the C-terminal domain. Superimposing both domains showed high similarity [8].

The active site is found in the cavity of the C-terminal domain with a volume of ~ 1000 Å³ [8]. Each subunit hosts only one heme *b*, which is embedded in a hydrophobic environment. The heme iron is coordinated by H160 on the proximal site which forms a hydrogen bonding bridge with E210 and K141. The iron atom exists in the ferric oxidation state (Fe(III)), the H-bonding network between H160, E210 and K141 plays an important part in the maintenance of this state [9]. Mutants E210A and K141E were used for studying this network, E210A is especially interesting because it mimics Cld-like proximal architecture [10]. On the distal site, R173 can be found which is suggested to play an important role in enzymatic turnover [8].

1.4.2 LmCld

So far, two crystal structures of LmCld were solved. One was crystallized without cofactor (apo-LmCld) [11] and the other with coproheme as a cofactor (coproheme-LmHemQ) [12].

One subunit of apo-LmCld consists of an N-terminal and C-terminal ferredoxin-like domain and resembles the subunit structure of NdCld. It crystallizes as a pentamer, unlike the hexameric assembly in solution [11]. The proximal side differs in having an alanine at the position of the glutamate, which stabilizes the position of the heme in functional Clds. On the distal side, a glutamine can be found instead of the catalytically important arginine [11]. Another notable difference to NdCld is the narrower access to the heme. This is due to a flexible stretch of amino acids which aligns with the substrate channel forming α-helix of functional Clds and has a big impact on the accessibility of the heme cavity since it is positioned in front of the binding site [11].

Coproheme-LmHemQ plays an important part in heme biosynthesis in Gram-positive bacteria by catalyzing the decarboxylation of two propionate groups of coproheme. It crystallizes in the same oligomeric state as apo-LmCld and the subunit A of both structures appears to be rather similar with a root-mean-square deviation of 0.233 Å [12]. There are two notable differences though: first, the orientation of two arginine residues (R133 and R179) at the substrate access channel exhibit different conformations in all subunits but chain A, and second, a longer bond length between the N of the

imidazole of the proximal histidine and the iron ion. The latter suggests, that the proximal histidine is not part of a hydrogen bond network [12].

1.4.3 CCld

So far, no crystal structure from CCld has been solved. The only clade 2 Clds which were characterized so far are from *Nitrobacter windogradskyi* (NwCld) [13] and *Klebsiella pneumoniae* [14]. Both form dimers in solution, have smaller subunit sizes than clade 1 Clds and show highly similar active sites.

1.5 Suggested mechanism of functional chlorite dismutases

1) $[PorFe(III)]^+ + [O\text{-}Cl\text{-}O]^- \rightarrow [PorFe(III)]^+\text{-}[O\text{-}Cl\text{-}O]^-$
2) $[PorFe(III)]^+\text{-}[O\text{-}Cl\text{-}O]^- \rightarrow [Por^{\bullet}Fe(IV)=O]^+ \cdots [O\text{-}Cl^{\bullet}]$
3) $[Por^{\bullet}Fe(IV)=O]^+ \cdots [O\text{-}Cl^-] \rightarrow [PorFe(III)]^+ + O=O + Cl^-$
4) $[PorFe(III)]^+\text{-}[O\text{-}Cl\text{-}O]^- \rightarrow [PorFe(IV)=O] \cdots [O\text{-}Cl^{\bullet}]$
5) $[PorFe(IV)=O] \cdots [O\text{-}Cl^{\bullet}] \rightarrow [PorFe(III)]^+ + O=O + Cl^-$

The reaction starts with the anionic chlorite attacking ferric heme *b* and formation of the Fe(III)-chlorite complex (Reaction 1). One of the Cl-O bonds is heterolytically cleaved and the ferric enzyme is oxidized, producing Compound I (oxoiron(IV) porphyrin cation radical) and the intermediate hypochlorite (Reaction 2). The latter nucleophilically attacks the ferryl oxygen, which results in the regeneration of Fe(IV) back to Fe(III) and the release of molecular oxygen and a chloride anion (Reaction 3) [15]. A conserved distal arginine (i.e. Arg127 in CCld) is supposed to play an important role in the stabilization of the substrate as well as the intermediate [5,8].

Besides this proposed mechanism, density functional theory calculations suggest the formation of Compound II (oxoiron(IV)) and chlorine monoxide (Reaction 4) through homolytic cleavage of chlorite [16,17]. Finally, chlorine monoxide recombines with Compound II (Reaction 5).

Previous studies showed a clear pH dependence for the chlorite degrading activity, while pH optima for NdCld and CCld were reported being pH 5.5 and pH 5.0, respectively [6,18]. The pH optimum for NdCld E210A and NdCld K141E is wild-type like [10]. It was shown that the distal arginine keeps the reaction intermediate hypochlorite in the active site and prevents its escape. So far it is believed that with increasing pH, the arginine is deprotonated and becomes incapable of fulfilling this function which leads to an inhibition of the enzyme by escaped hypochlorite and thus to a decrease of chlorite degradation activity [18].

2 Aim of thesis

The goal of this work was the biochemical, biophysical and structural characterization of NdCld wt, NdCld K141E, NdCld E210A, LmCld wt and CCld wt. Different methods were applied to achieve this goal:

- Polarographic measurements using a Clark-type electrode for determining steady-state kinetics.
- Electronic circular dichroism spectroscopy (eCD) to compare secondary structures and determine unfolding properties.
- Stopped-flow spectroscopy for determining pre-steady-state kinetics.
- UV-vis and fluorescence spectroscopy for determining (un)folding properties of the protein and to analyze ligand binding.
- X-ray crystallography for determining the three-dimensional structure.

3 Material and Methods

3.1 Expression and purification

CCld was produced in *E. coli* strain BL21 (DE3) Gold containing the pET52b+ vector. LmCld was produced in E. coli Tuner (DE3) cells containing the pET21(+) expression vector. NdCld was produced in E. coli Tuner (DE3) cells containing the pET-21b(+) vector. All vectors contain the DNA fragment of Cld (from *Cyanothece* sp. PCC7425, *Listeria monocytogenes* or "*Candidatus* Nitrospira defluvii*",* respectively), which is under the control of a T7 promoter. They also contain a *lac* operon which makes it possible to induce the expression of Cld with the artificial compound isopropyl β-D-1-thiogalactopyranoside (IPTG). Other features include an ampicillin resistance, an N-terminal strep-tag II (for purification purposes) and a human rhinovirus HRV 3C protease cleavage site to get rid of the strep-tag II for crystallization trials.

A cryoculture was used to inoculate 10 ml lysogeny broth medium (LB medium) supplemented with 100 µg/ml ampicillin (Amp-LB). Cells were grown overnight at 37°C. On the next day, 2 ml-aliquots of this overnight-culture (o/n-culture) were used to inoculate 500 ml of Amp-LB. Cells grew roughly 4 h until an OD_{600} of 0.6 to 0.8 was reached, then hemin was added (50 mg/l) and the shaker was set to cool down to 16°C. After 30 minutes, protein expression was induced with IPTG (0.5 mM). On the next day, the cells were harvested by centrifugation for 20 min at 3400 g and 4°C. The supernatant was discarded and the pellets transferred into a falcon tube and frozen at -80°C. The procedure described above is valid for CCld and was slightly varied for the other proteins (for NdCld 1 ml aliquots were used for inoculating 500 ml of Amp-LB and the harvesting step was started 4 h after induction with IPTG and for LmCld temperature was lowered to 24°C and the harvesting step was started 4 h after induction with IPTG).

For purification, frozen cells were thawed and 40 ml lysis buffer together with 200 µl phenylmethanesulfonylfluoride (PMSF) was added to the pellet (originating from 1000 ml cell suspension). After thoroughly shaking the suspension, the cells were broken using an ultra sonicator (3 x 60 sec, 50% pulse). The resulting mixture of cell contents was then centrifuged (20000 g, 40 min) to separate Cld molecules from cell membranes and other macromolecules (especially DNA) and finally obtain it in the supernatant. The pellet was discarded, the supernatant vacuum-filtrated (0.45 µm) and afterwards used for affinity chromatography. For that, a StrepTrap HP - column (5 ml, GE Healthcare) was first washed with 5 column volumes (CV) of water (1 ml/min) and afterwards equilibrated with 5 CV of binding buffer (1 ml/min) using the ÄKTA system. The sample was then applied to the column

(1 ml/min) and afterwards washed with binding buffer (1 ml/min) until the UV-signal stayed constant. Bound Cld was then eluted with elution buffer containing 1 mM d-desthiobiotin (1 ml/min) and fractionated in 2 ml-fractions using an ÄKTA fraction collector. Fractions containing CCld were then pooled and concentrated using Amicon-tubes with a cutoff of 10 kDa. After 5 rounds of centrifugation (20 min, 4500 g) and adding potassium phosphate buffer (50 mM, pH 7.0) after every round, the Cld-enriched retentate was used for concentration determination via UV-vis spectroscopy.

Chemicals, solutions and instruments:

Table 3.1: Media and buffers.

LB-medium	Lysis buffer	Binding buffer	Elution buffer
5 g/l yeast extract	50 mM HEPES pH 7.4	20 mM HEPES pH 7.4	20 mM HEPES pH 7.4
10 g/l peptone	5% glycerol	5% glycerol	2% glycerol
10 g/l NaCl	0.5% Triton X-100		1 mM d-desthiobiotin
	0.5 mM EDTA (Ethylenediaminetetra-acetic acid)		
	1 mM PMSF		

Table 3.2: Reagents.

IPTG stock	Ampicillin stock	PMSF stock	Hemin stock
1 M in H_2O	100 mg/ml in H_2O	34.8 mg/ml in 100% EtOH	5 g/l in NaOH and H_2O

3.2 Biochemical/biophysical studies

3.2.1 Spectroscopic determination of protein concentration

The concentration of the purified heme protein was determined spectroscopically using an Agilent 8453 Diode Array UV-vis spectrophotometer. First, water was measured as a blank followed by an appropriate dilution (i.e. absorbance <1) of Cld. Two main absorption peaks could be observed: the protein peak at 280 nm which originates from aromatic amino acids like tryptophan, and the Soret peak, which originates from an electron dipole movement in the porphyrin-ring that allows π-π^* transitions [19]. Using Lambert-Beer's law $A = \varepsilon * c * d$ (where A is the absorption of the solution, ε the molar absorption coefficient [M^{-1} cm^{-1}], c the concentration of Cld in solution [M] and d the diameter of the cuvette [cm]), one can calculate the concentration of the protein containing heme using the absorption at the Soret maximum with an estimated molar absorption coefficient of 100000 M^{-1} cm^{-1}.

Another important value is the Reinheitszahl, which is calculated as A_{Soret}/A_{280}. It represents the ratio of Cld with and without heme cofactor and the purity of the sample in the solution. After spectroscopic determination of concentration, aliquots of Cld were frozen and stored at -80°C until further use.

3.2.2 Steady-state kinetics of chlorite degradation of NdCld measured with a Clark-type electrode

The Clark-type electrode (see Figure 3.1) is an O_2-sensitive instrument which can measure oxygen saturation polarographically. Two electrodes are connected via an electrolyte solution in the following manner: Both, silver anode and platinum cathode are embedded into an epoxy resin disc (A). The cathode can be found at the center of a little dome (B), which is surrounded by a well in which the anode (C) is built. The well also contains the electrolyte, which stays in contact with the cathode through a paper spacer and polytetrafluoroethylene membrane. The membrane is fixed by an O-ring around the dome, also an outer O-ring groove (D) surrounds the apparatus. The electrode measures a current at a constant polarizing voltage which is directly proportional to the partial pressure of oxygen in the solution (located in the borosilicate glass reaction vessel).

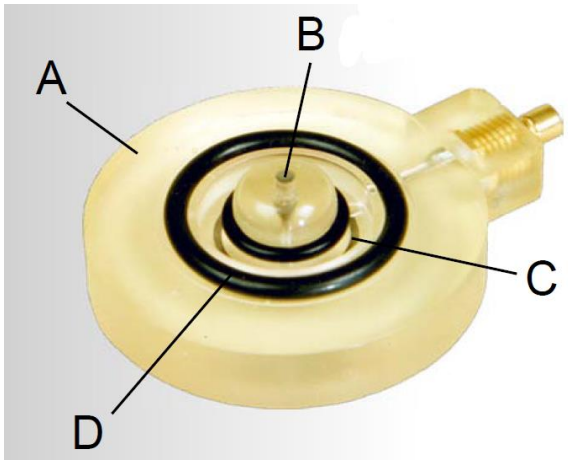

Figure 3.1: Illustration of a Clark-type electrode [20]. (A) Epoxy resin disc, (B) cathode at center of dome, (C) anode, (D) O-ring groove.

Cathode: $O_2 + 4H_3O^+ + 4e^- \rightarrow 6H_2O$

Anode: $4Ag + 4Cl^- \rightarrow 4AgCl + 4e^-$

total: $4Ag + 4Cl^- + 4H^+ + O_2 \rightarrow 4AgCl + 2H_2O$

The temperature has to be held constant during the measurement since the solubility of oxygen in liquids is temperature-dependent. This is achieved through a direct connection of the electrode mantle to a water bath, purging the electrode with water (30°C).

It is possible to measure the produced oxygen since functional chlorite dismutases catalyze the following reaction:

$$ClO_2^- \rightarrow O_2 + Cl^-$$

Before the measurement can be started, the electrode has to be calibrated. This was done with O_2 (100% O_2 saturation) and N_2 (0% O_2 saturation). All solutions except the enzyme were then pipetted into the reaction vessel, in which a stirrer guarantees the proper mixing of all components. Additionally, before each individual measurement, the liquid in the measurement chamber has to be oxygen-free, which was achieved by flushing with N_2. Then the lid was closed, the enzyme was applied with a Hamilton syringe and the increase in oxygen concentration was recorded with the associated software on a PC. All measurements were carried out twice, the arithmetic mean was determined afterwards. After drawing a Hanes plot it is possible to calculate the kinetic parameters K_M, V_{max}, k_{cat} and k_{cat}/K_M using its slope k and intercept d:

- The Michaelis-Menten constant $K_M = d*V_{max}$ describes the amount of substrate needed for the enzyme to obtain half of its maximum rate. It can be seen as an approximate measure of the affinity of the enzyme for the substrate.
- $V_{max}= 1/k$ is the theoretical maximum reaction rate.
- The turnover number $k_{cat}= V_{max}/E_0$ is the maximum number of substrate molecules that an enzyme can convert to product per unit of time for a given enzyme concentration (E_0).
- k_{cat}/K_M describes the overall efficiency of the enzyme for a given substrate and it is used to compare two enzymes acting on the same substrate. Its upper limit is the diffusion rate.

<u>Chemicals, solutions and instruments:</u>

Here, the reactions of NdCld K141E and NdCld E210A with different concentrations of chlorite at pH 5.5 and pH 9.0, respectively, were studied. The initial velocity (v_0) was then calculated by defining the slope at the beginning of the reaction, using the software “Oxygraph”. The following concentrations were used:

- Buffers
    - 50 mM citrate phosphate buffer pH 5.5
    - 50 mM Tris/HCl buffer pH 9.0
- $c_{ClO_2^-}$: 5 µM, 15 µM, 20 µM, 50 µM, 100 µM, 200 µM, 300 µM, 400 µM, 600 µM, 1000 µM
- c_{enzyme}: 20 nM. The actual concentration was determined spectroscopically after the final dilution step.

- Clark-type electrode (Hansatech Oxygraph 11125)
- Thermostat (Medingen E5)
- 50 µl syringe (Hamilton)

3.2.3 Electronic circular dichroism spectroscopy

Electronic circular dichroism spectroscopy is a method which utilizes the interactions of linearly polarized electromagnetic waves with an optically active medium. It further measures the ellipticity of the wave after it has passed the medium. Electromagnetic waves are synchronized oscillations of electric and magnetic fields, while the magnetic field is always perpendicular to the electric field. Polarization makes the electric field oscillate in only one direction resulting in linearly polarized light. Superposition of two waves with same amplitude and wavelength, but phase difference of 90 degrees will result in right circularly polarized light while left circularly polarized light will be obtained if the phase difference equals minus 90 degrees [20].

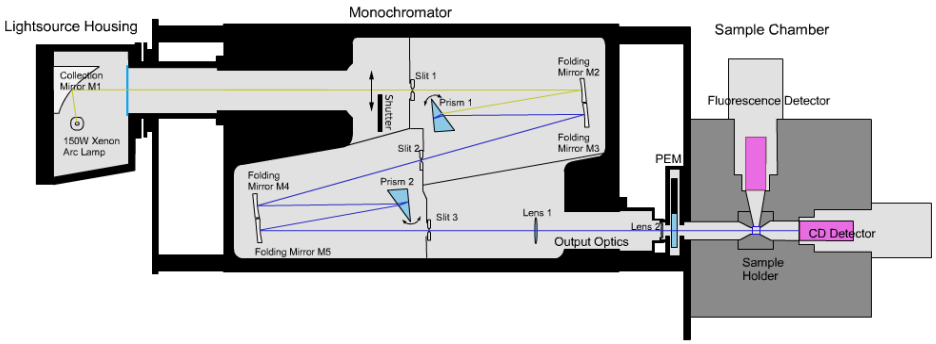

Figure 3.2: Schematic representation of a CD spectrophotometer [20].

Some substances absorb left circularly polarized light to a different extent than right circularly polarized light, which is called circular dichroism. A linearly polarized wave can be seen as a superposition of left and right circularly polarized light. When it enters a medium which exhibits circular dichroism, the wave properties (such as amplitude and wavelength) will change to a different extent, which finally results in an elliptically polarized wave in which the field vector rotates along an ellipsoid path.

A CD spectrophotometer (see Figure 3.2) consists of a light source (e.g. xenon lamp), a monochromator, a linear polarizer, a photoelastic modulator (PEM), a sample holder and a detector with an appropriate signal processing system. The detector measures the absorption of left and right circularly polarized light, from which ellipticity is calculated. There are several optically active materials, e.g. carbon atoms with four different substituents, disulfide bonds, aromatic side chains or certain prosthetic groups (including heme *b*).

Signals in the far UV region (180 nm – 250 nm) reveal information about secondary structure elements of the protein sample, the main absorption in this region is due to the peptide bond. The near UV region (250 nm – 340 nm) gives a tertiary structure also called fingerprint region which arises from the aromatic amino acids phenylalanine, tyrosine and tryptophan. The visible region (340 nm – 800 nm) is ideal for studying the binding site of organic cofactors (like heme), since they show strong signals when bound to the protein. It is also possible to record a melting curve, using a defined temperature interval at a particular wavelength. This makes it possible to study folding, unfolding and refolding properties of a protein.

Here, NdCld and its mutants as well as LmCld have been studied using eCD. Measurements were done as follows: After measuring the baseline with buffer, full spectra of the respective enzyme were recorded at 20°C (180 nm – 260 nm for far UV and 260 nm – 500 nm for near UV and UV-vis) and baseline correction was performed. The wavelength was then fixed appropriately and the temperature was increased to 85°C at a rate of 1°C min^{-1}, followed by measuring a full spectrum at 85°C and, after cooling down, recording a spectrum at 20°C again. The spectral bandwidth was set to 3 nm and the scan speed to 10 s nm^{-1}. The calculation of secondary structure elements for NdCld was done using the program CDNN [21].

Chemicals, solutions and instruments:

- Buffers:
    - 5 mM citrate phosphate buffer pH 4.0
    - 5 mM citrate phosphate buffer pH 5.5
    - 5 mM potassium phosphate buffer pH 7.0
    - 5 mM glycine/NaOH buffer pH 10.0
- c_{enzyme}: 5 µM
- ChirascanTM CD Spectrometer (Applied Photophysics) including Peltier element for temperature control
- Cuvettes with 1 mm (far UV) and 1 cm (near UV and UV-vis) pathlength

3.2.4 Chemical unfolding of CCld measured by fluorescence spectroscopy

For proteins to carry out their function, it is essential that they are properly folded. This information is encoded in their amino acid sequence. The interactions which play an important role during protein (un)folding are hydrogen bonds, disulfide bridges, electrostatic interactions and hydrophobic effects. Since the biological activity is strongly related to the protein's three-dimensional structure, it is an important goal to better understand this process. Studying the intrinsic fluorescence properties of a

protein is one possibility to do that. Tryptophan, tyrosine and phenylalanine fluoresce when excited, but just the former two are used because of their high quantum yields. Their properties change strongly depending on their environment. In the native state of a protein, tryptophan and tyrosine residues are usually found in the hydrophobic core of a protein, when denatured, they become exposed to the solvent. There are different ways to denature a protein, like changing temperature or adding chaotropic reagents.

Here, CCld was supplemented with increasing concentrations of guanidine hydrochloride (GdnHCl) and incubated for 24 h. Each mixture was measured with the fluorescence spectrophotometer using an excitation wavelength of 295 nm (to selectively excite tryptophan), emission wavelength range of 300 nm to 450 nm and a slit of 2 nm. The concentration of GdnHCl was then plotted against the fluorescence at 350 nm and against $\Delta G^0_{N\rightarrow D}$(calculation see chapter 4.2.2) to determine the *m*-value, which is derived from the slope of the corresponding linear fit, and ΔG_{H_2O}, which can be obtained from the intercept. c_m is the concentration of GdnHCl at which $K_{eq} = 1$ (where K_{eq} is the equilibrium constant). It is determined via extrapolation.

To gain further information about the heme cavity, the reaction mixtures were also analyzed using UV-vis spectroscopy. Measurements were carried out in a wavelength range of 250 nm -700 nm with a slit of 2 nm. The concentration of GdnHCl was then plotted against the absorption at 407 nm (Soret maximum) and against $\Delta G^0_{N\rightarrow D}$ and the unfolding parameters were calculated as described above. The unfolding curves can then be used to compare partially/fully unfolded protein with the native structure.

Meaning of the unfolding parameters:

- The *m*-value is the derivative of the change in stabilization free energy upon the addition of denaturant.
- The conformational stability ΔG_{H_2O} is the free energy difference between the native folded state and unfolded state in water.
- c_M represents the concentration of denaturing agent, at which 50% of the protein is folded/unfolded.

Chemicals, solutions and instruments:

CCld was supplemented with increasing concentrations of GdnHCl and, for the unfolding to reach equilibrium, measured after 24 h. The following concentrations were used:

- Buffers:
    - 50 mM potassium phosphate buffer pH 7.0

- c_{GdnHCl}: 0.005 M, 0.01 M, 0.025 M, 0.05 M, 0.075 M, 0.1 M, 0.2 M, 0.5 M, 0.8 M, 1 M, 2 M, 2.5 M, 3 M, 3.5 M, 4 M
- c_{enzyme}: 0.5 µM
- Fluorescence spectrophotometer Hitachi F-7000
- Spectrophotometer Hitachi F-7000
- 10 mm quartz cuvette

3.2.5 Pre-steady-state kinetics of LmCld titrated with cyanide and determined by conventional stopped-flow spectroscopy

The stopped-flow technique is a highly sophisticated method which allows to measure spectroscopic properties of two reagents just milliseconds after they are mixed. Due to this, it is possible to measure an enzyme reaction prior to equilibrium in the so-called pre-steady-state. The apparatus consists of a mixing device, a measurement chamber, a detection and recording system and a stop syringe. The reagents are applied via drive syringes. For a graphical representation of the instrumentation see Figure 3.3. The reaction starts by pushing the liquids out of the drive syringes mechanically, which causes them to mix, to enter the measurement chamber and subsequently the stop syringe. A small movement of the stop syringe activates a mechanical stop which prevents further mixing and triggers the UV-vis detection and recording system. Until the mixed liquids reach the measurement chamber nothing can be recorded, the very short time interval (usually around 1 ms) is called the dead time. The performance of the stopped-flow apparatus is largely dependent on the dead time which can also be seen as the age of the reaction as it enters the measurement chamber.

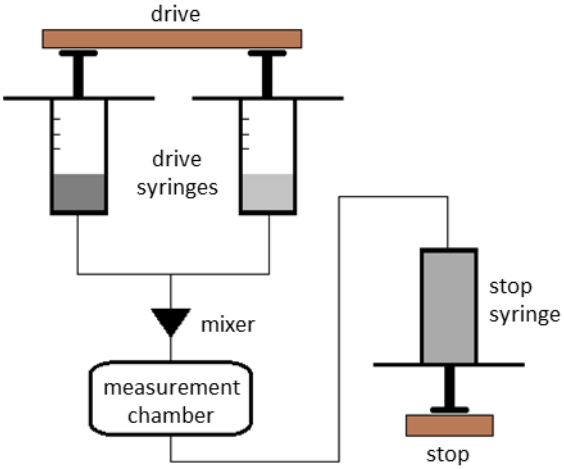

Figure 3.3: Design of a stopped-flow apparatus.

For this work, stopped-flow spectroscopy was used to determine the behavior of cyanide as a ligand of LmCld. Cyanide can be used as probe to test the accessibility of the heme cavity. Also, the bound cyanide complex mimics higher oxidation states like Compound I. Before starting the measurements, high quality water (HQ-H_2O) was used to purge the apparatus. The syringes were then filled with cyanide and enzyme solutions and the first series of measurements was started using the following parameters:

- Wavelength: 200-750 nm (photodiode array)
- Time period: 10 s
- Time points: 100

Three different concentrations of cyanide were measured (10 µM, 100 µM, 1000 µM) and mixed with LmCld to record the typical redshift of the Soret maximum upon binding of cyanide and to determine the maximum absorbance of the Fe-CN complex. After that, a second series of measurements was started using the following parameters:

- Wavelength: 412 nm (monochromator)
- Time period: 10 s
- Time points: 1000

Six different concentrations of cyanide were measured (100 µM, 200 µM, 300 µM, 400 µM, 500 µM, 750 µM). Each measurement was repeated 3 times. The optical quartz cell had a pathlength of 1 cm and a volume of 20 µl. Enzyme and cyanide were mixed in a 1:1 ratio. After determining the arithmetic mean, a single exponential fit of the time trace was applied to obtain the k_{obs} value for each concentration. These k_{obs} values were then plotted against the cyanide concentrations and after applying a linear fit, k_{on} and k_{off} could be read out of the slope and the intercept, respectively, and finally $K_D = k_{off}/k_{on}$ was calculated. All measurements were done at 25°C.

Meaning of the parameters:

- k_{on} is the association rate constant.
- k_{off} is the dissociation rate constant.
- $K_D = k_{off}/k_{on}$ is the equilibrium binding constant.

Chemicals, solutions and instruments:

- Buffers:
    - 100 mM potassium phosphate buffer pH 7.0
- c_{CN^-}: 100 µM, 200 µM, 300 µM, 400 µM, 500 µM, 750 µM
- c_{enzyme}: 5 µM
- Stopped-flow spectrometer (model SX- 18MV, Applied Photophysics)
- Software: Acorn PiStar-180
- Monochromator
- Photodiodearray (Applied Photophysics)
- 2 ml disposable syringes (Braun)

3.2.6 Titration of NdCld and CCld with potential ligands followed by UV-vis spectroscopy

In Clds, ferric Fe(III) is coordinated by the four nitrogen atoms of the porphyrin ring and the proximal histidine. At the distal side, an H_2O molecule is usually weakly bound at pH 7.0 [8,13]. This leaves the octahedral system in the high-spin state (S=5/2) with H_2O being the high-spin ligand. Other ligands, e.g. CN^-, replace the relatively weakly bound H_2O and create a low-spin state (S=1/2). To study the behavior and possible change of spin states, NdCld and CCld were titrated with certain ligands. The changing of spin-states can be analyzed spectroscopically with the help of the two Q-bands (Q_O and Q_V, as low-spin markers) and the charge transfer band (CT1) as a high-spin marker (see Fig. 4.1). They arise/elapse according to the concentration of the bound ligand. Also, a pronounced redshift of the Soret maximum can usually be observed when a low-spin complex is generated. CCld/NdCld was supplemented with increasing concentrations of the respective ligand (F^-, NO_2^-, SCN^-) and spectra were recorded in a wavelength range of 250-700 nm. A fit, described by the equation y=ax/(b+x) (rectangular hyperbola), was then applied at a chosen wavelength using the software SigmaPlot Version 10.0 and the K_D-values were calculated.

Chemicals, solutions and instruments:

- Buffers:
    - 50 mM 2-(N-morpholino)ethanesulfonic acid-buffer (MES-buffer) pH 5.5
    - 50 mM potassium phosphate buffer pH 7.0
- c_{ligand}: 8 µM, 47 µM, 432 µM, 836 µM, 1.62 mM, 2.01 mM, 2.4 mM, 2.79 mM, 3.18 mM, 3.96 mM, 5.5 mM, 7.04 mM, 10.07 mM, 13.05 mM, 16.7 mM, 37.76 mM, 50.56 mM, 65.04 mM, 90.7 mM, 112 mM

- c_{enzyme}: 2 µM
- Software: SigmaPlot version 10.0
- Spectrophotometer Hitachi F-7000
- Specord Zeiss S10
- 10 mm quartz cuvette, constant stirring at 25°C

3.3 Structural studies using X-ray crystallography

X-ray crystallography is a powerful tool in structural biology. Besides nuclear magnetic resonance (NMR) spectroscopy and cryo-electron microscopy, it is used to determine the three-dimensional structure of a macromolecule. Since the first crystal structures were solved in the 1950s, it had a big impact on the development of many scientific fields.

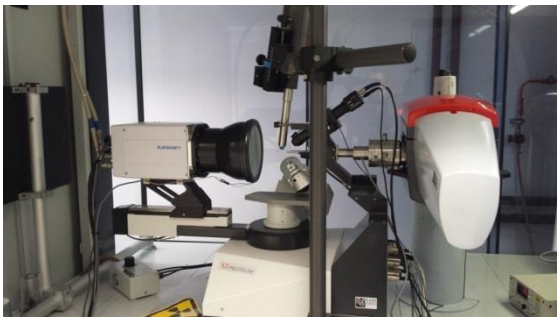

Figure 3.4: In-house X-ray machine at Max. F. Perutz Laboratories Vienna.

Biological macromolecular crystallography requires the generation of protein crystals. Crystallisation occurs in oversaturated solutions, which can be divided into three regions of increasing probability of nucleation and precipitation (see Figure 3.5). The formation of a critical nucleus (which is a prerequisite to start crystallisation) poses a large energy barrier. Oversaturation is the driving source to overcome the activation barrier.

The empirical process of finding the right crystallisation conditions can be very time consuming, since a lot of crystallizing agents exist which can be used in different combinations. Until now, it is impossible to predict the crystallizing conditions of a distinct protein. However, commercially available screens facilitate the screening process.

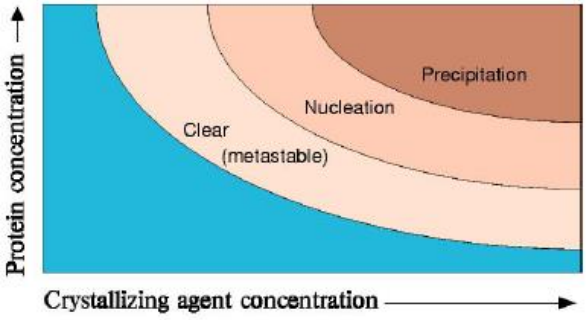

Figure 3.5: Crystallization phase diagram [22].

Nowadays, vapour diffusion is the most commonly used method to grow protein crystals. In a closed system, a droplet containing a mixture of the protein and the crystallizing liquid equilibrates against a

larger reservoir of crystallizing liquid. Therefore, the concentration of the protein and the crystallizing agent in the droplet rises, which leads to supersaturation. Crystals begin to grow when the protein reaches the nucleation phase (see Figure 3.5) and, as a consequence, the concentration of protein in solution will decrease. Crystal growth ceases at the boarder of the metastable region. Usually, vapour diffusion can be executed as hanging drop or sitting drop (see Figure 3.6).

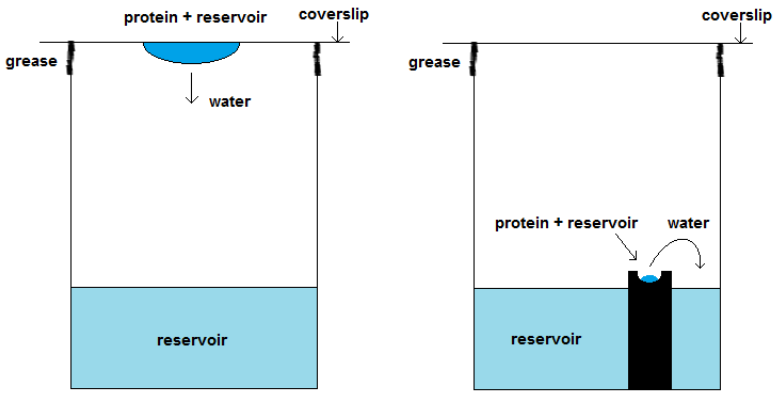

Figure 3.6: Visualization of the hanging drop- (left) and sitting drop technique (right).

Once the proper crystallizing condition for the protein is found and crystals are available, they can be used for diffraction experiments (see Figure 3.7). A beam of incoming X-rays is scattered by the electrons in the crystal. From the resulting diffraction pattern it is possible to calculate the electron density. For this, a mathematical function called Fourier transform is used which needs the wavelength of the initial X-ray beam, the intensity of the diffracted spots and the phase angles. It is physically impossible to measure the phase angles, which is commonly known as the "phase problem". Solving the "phase problem" is an important issue which is nowadays realized with the help of different methods, for example molecular replacement.

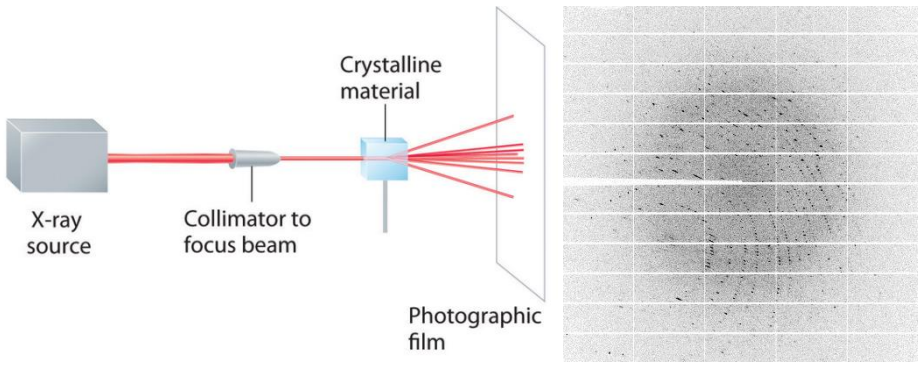

Figure 3.7: Visualization of the diffraction experiment (left) [22]. Diffraction image of CCld on in-house X-ray machine (right).

After the electron density is obtained, its interpretation leads to the generation of a model of the investigated protein. The model usually has to be corrected or "refined", since phases are only approximate and may be stuck in a mathematical local minimum, instead of a global optimal solution. Refinement involves alternating round of either automated optimization of all relevant parameters and/or manual corrections to interpret the experimental data well enough [23]. In reality, crystallographic models of macromolecules are very complex and need a lot of parameters to refine which basically means, that the number of observations is usually not enough. Because of that, refinement is carried out using stereochemical restraints to incorporate distinct properties of the real protein [23]. For instance, the angles of N-Cα-C in the protein backbone have a wide distribution but not all are stereochemically possible. Data quality statistics can be calculated which assist in the refining process i.e. R_{free} and R_{work}. Introduction of too many model parameters would tend to replicate the errors of the data which leads to overinterpretation and is reflected by a significantly high R_{free} in respect to R_{work} [23].

To conclude, several programs are being used for refinement, such as the widely used REFMAC [24] but also the PHENIX suite [25], which offers a huge selection of adjustable options and is being used in the course of this thesis. After refinement is completed, the structural model of the protein can be deposited in the protein databank (PDB).

3.3.1 Preparation of samples

Purified CCld was thawed, pooled in one reaction container and digested o/n at 4°C with HRV3C-protease at a ratio of 1:10 to cut the strep-tag II from the protein. The resulting solution was then applied on a size exclusion chromatography (SEC) column (Superdex 16/60 200 pg, GE Healthcare Life Sciences) with two affinity columns in front:

1. GSTrap HP - column (GE Healthcare) to retain HRV3C-protease.
2. StrepTrap HP - column (GE Healthcare) to retain uncut protein and the removed strep-tag II.

Prior to protein application, the system was equilibrated with 20 mM potassium phosphate buffer pH 7.0. After this final polishing step, the protein solution was concentrated using ultra-centrifugal filters (Amicon) with a molecular weight cut-off of 10000 Da to a concentration of about 7 mg/ml. The sample was then ready for crystallization trials.

3.3.2 Crystallization

Initial crystallization trials were done by sitting drop vapor diffusion in 96-well plates (MRC Crystallization plate) using commercially available screens. Crystallization drops were set using a

Phoenix HT crystallization robot. The reservoir was filled with 40 µl crystallant solution. In the sample wells ratios of 150:200 nl, 200:200 nl and 250:200 nl of protein to crystallant were dispensed. For optimization of crystallizing conditions an Alchemist II liquid handling robot (Rigaku) was used for dispensing non-commercial optimization screens in 96 deep-well plates (Eppendorf). All plates were inspected by the Ministrel DT imaging system (Rigaku) equipped with the Atlantis software for automatic imaging in combination with the CrystalTrak software (Rigaku).

After setting up 96-well plates for commercial screens using the JCSG-plus™ (Molecular Dimensions)- and PEGRx-Screens it lasted 1-2 weeks until crystals started to grow, during which they were stored in a temperature-regulated room (22°C). After 3-4 weeks crystals were fished, cryoprotected, flash frozen, stored in liquid nitrogen and then shipped to the European Synchrotron Radiation Facility (ESRF) [26].

Additionally, 24-well plates (Linbro plate; Crystalgen) were set up for non-commercial optimization screens for which the hanging drop vapor diffusion technique was chosen. This setup allows a bigger drop size and more drops per well. With that, more or even bigger crystals can possibly grow. Each well contained 1-3 drops, each consisting of 2 µl protein and 1.3 µl ML. 300 µl – 500 µl of ML was used as reservoir solution. After 3-4 weeks crystals were fished, cryoprotected, flash frozen, stored in liquid nitrogen and then shipped to European Synchrotron Radiation Facility (ESRF) [26].

3.3.3 Crystal soaking

Additionally, soaking experiments were performed. Depending on the respective crystallizing condition, the necessary ingredients were thoroughly mixed with HQ-water and appropriate crystals were then supplemented with this solution. It included 10 mM of the soaking agent and the final concentration of the cryoprotectant was 25% (v/v) (see Table 3.3).

Table 3.3: Soaking experiments.

Number	Crystallizing condition	Cryoprotectant	Soaking agent
1	0.09 M $MgSO_4$, 0.1 M MES pH 6.5, 22% (v/v) PEG 3350	25% (v/v) MPD	10 mM thiocyanate
2	1.45 M $MgSO_4$, 0.1 M MES pH 6.5, 5% (v/v) Glycerol	25% (v/v) Glycerol	10 mM fluoride

3.3.4 Anomalous scattering

It is possible to identify certain elements in the electron density map by adjusting the wavelength of the incident photons in the diffraction experiment. The result is an anomalous diffraction pattern. Up to a certain energy threshold the incident photon is either scattered or not, but never absorbed. For

photons which reached that threshold three ways are possible: the photon is scattered normally, it is absorbed and reemitted at lower energy or it is absorbed and reemitted at the same energy but with different phase. The latter is mathematically described by adding an imaginary component to its phase and can be visualized by plotting electron energy vs. absorption/fluorescence. Anomalous scattering depends on the incident wavelength and the element to be examined. (see Figure 3.8) [27].

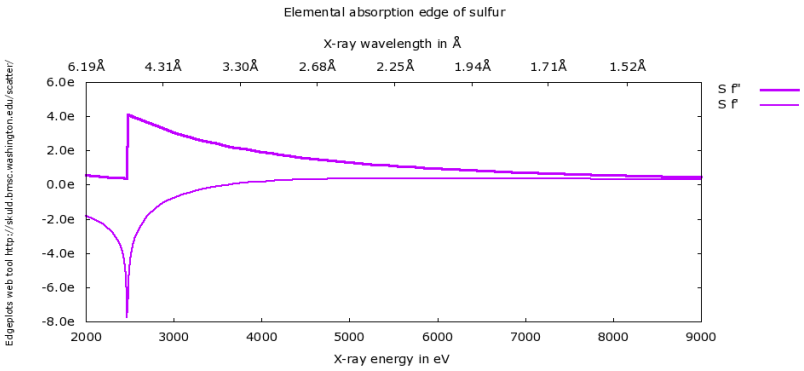

Figure 3.8: Absorption edge of sulfur with f' representing the absorption and f'' representing the imaginary component. The plot was calculated using the subroutine library by Brennan and Cowan [28].

3.3.5 X-ray diffraction and data collection

X-ray diffraction was done at ESRF at various beamlines. XDS [29,30] was used to process the data. Anomalous datasets (used for highlighting sulfur, see chapter 3.3.4) were collected in-house on a Bruker Microstar rotating anode at a wavelength of 1.54 Å and processed using the Proteum2 software suite.

3.3.6 Phasing

The phases for early data sets were obtained by molecular replacement using the molecular-replacement pipeline Balbes [31]. After finishing the refinement of the first structure it was used for molecular replacement for following structures. Phases for 1.54 Å in-house datasets were found using single wavelength anomalous dispersion (SAD) with the help of AutoSol [32].

3.3.7 Refinement

The structure of CCld was refined using the software programs phenix.refine of the PHENIX software package, and TLSMD [33]. Manual model building was performed using COOT [34,35], while validation of the model was done using the MOLPROBITY program [36,37]. Additionally, the PDB-REDO server was used [38].

Refinement included the following steps:

1. Model building with special emphasis on terminal ends and loops. Regions of very poor electron density (flexible loops) were left out.
2. Finding alternative configurations.
3. Adjusting rotamers, optimizing the geometry and elimination of Ramachandran-outliers throughout the molecule.
4. Insertion of ligands.

Protein atoms were refined anisotropically in all structures while water molecules were refined isotropically for native CCld and CCld in complex with fluoride, and anisotropically for CCld in complex with thiocyanate. Hydrogens were not refined in any structure.

4 Results and Discussion

4.1 Recombinant protein expression and purification

In Figure 4.1 typical UV-vis spectra of studied Clds at pH 7.0 are shown.

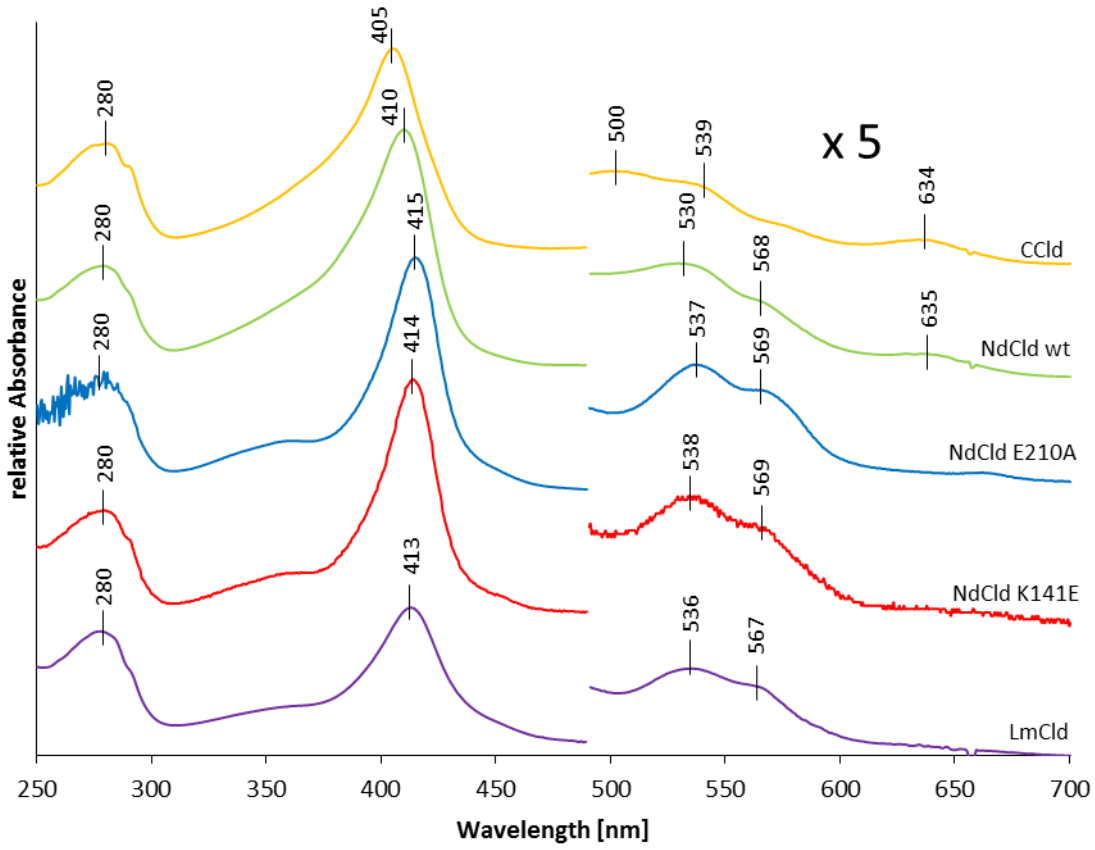

Figure 4.1: UV-vis spectra of studied Clds at pH 7.0.

The spectra show Soret maxima between 405 nm and 413 nm while it is noteworthy that both mutants NdCld E210A and NdCld K141E have redshifted peaks compared to NdCld wt. Q-bands can be found around 537 nm and 569 nm with the exception of CCld which shows Q-bands at 500 nm and 539 nm. Both NdCld mutants and LmCld do not show any absorbance in the CT region. CT bands are typical for high-spin heme proteins and are located within the range 610-650 nm [9]. CCld and NdCld wt show CT maxima at 634 nm and 635 nm, respectively, and indicate a pronounced high-spin character.

NdCld appeared to be a pentamer in solution with a molecular mass of approximately 130 kDa [8]. It yielded up to 5 mg per 1 L of culture. The Reinheitszahl R_Z was calculated to be approximately 2.0.

LmCld proved to be a hexamer in solution with a molecular mass of 180 kDa [11]. It yielded around 5 mg per liter of culture with an approximate R_Z of 1.1 which is rather low compared to NdCld and CCld [11].

CCld was shown to be a dimer in solution with a molecular mass of approximately 24 kDa [6]. 1 L of culture yielded around 3 mg of protein. The Reinheitszahl was calculated to be approximately 1.8.

4.2 Biochemical and biophysical studies

4.2.1 Steady-state kinetics of chlorite degradation of NdCld measured with a Clark-type electrode

Chlorite dismutases catalyze the decomposition of chlorite into chloride and dioxygen. This can be measured polarographically with O_2-sensitive electrodes such as a Clark-type electrode. It is important to only use the initial linear phase for the calculation of steady-state parameters because with increasing substrate concentration chlorite dismutases are inhibited by hypochlorite, which is an intermediate during enzyme turnover (see Figure 4.4) [18]. Initial velocities v_o were obtained from initial linear time traces. After drawing a Hanes-Plot (see Figure 4.2 and Figure 4.3) and applying a linear fit, it is then easily possible to calculate steady-state parameters such as K_M, k_{cat} and k_{cat}/K_M (see below for an exemplary calculation). Initial velocities showed a very similar behavior for both mutants at pH 9.0 while they were significantly higher at pH 5.5 (see Figure 4.4).

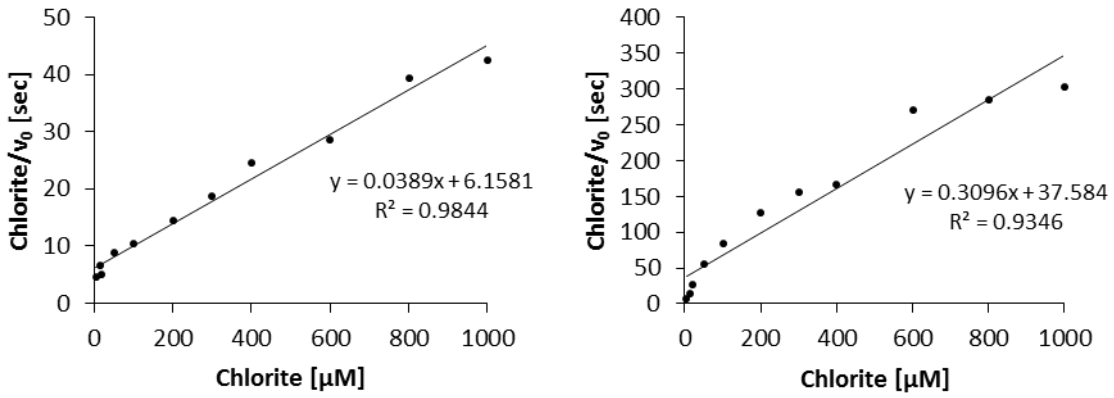

Figure 4.2: Hanes plots of NdCld E210A with linear fits at pH 5.5 (left) and pH 9.0 (right).

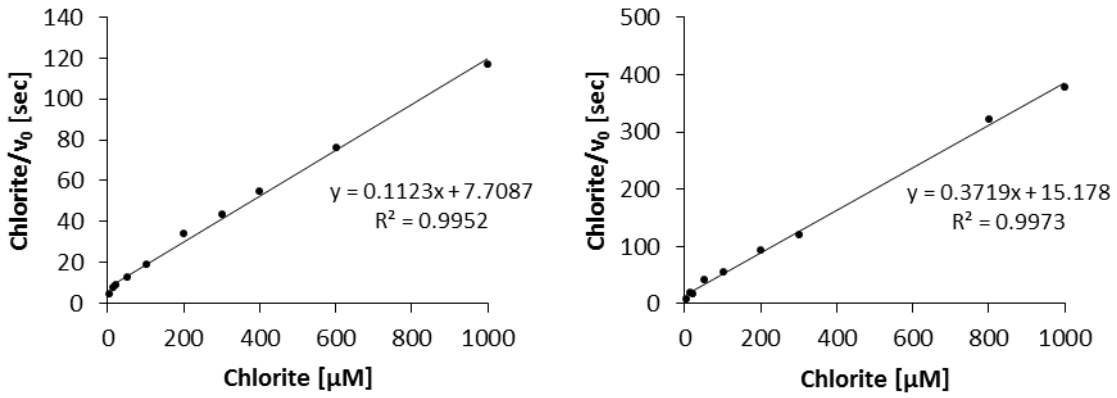

Figure 4.3: Hanes plots of NdCld K141E with linear fits at pH 5.5 (left) and pH 9.0 (right).

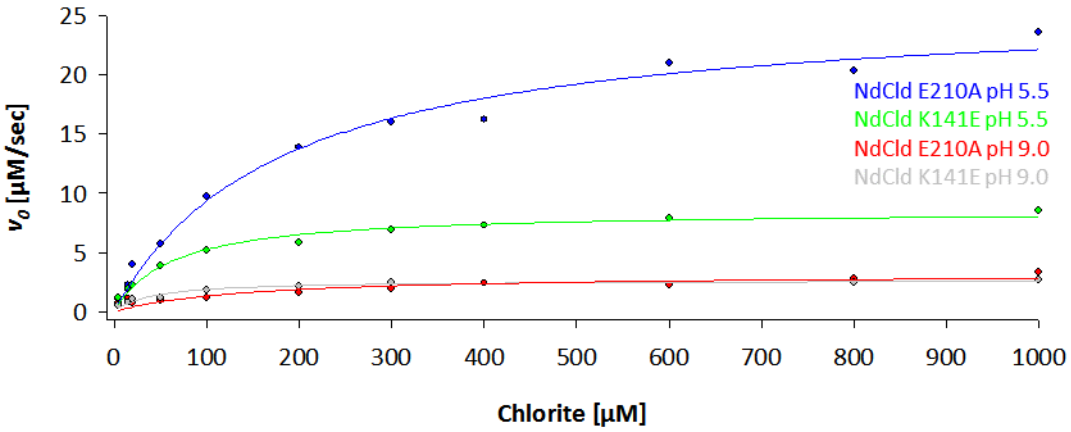

Figure 4.4: Chlorite vs v_0 of NdCld E210A and NdCld K141E fitted with rectangular hyperbolic functions at pH 5.5 and pH 9.0.

Exemplary calculation of catalytic parameters of NdCld E210A at pH 5.5:

$$V_{max}=\frac{1}{k} \quad K_M=d*V_{max} \quad k_{cat}=\frac{V_{max}}{E_0}$$

$$k=0.0389\ \frac{sec}{\mu M} \quad d=6.1581\ sec \quad E_0=0.142\ \mu M$$

$$V_{max}=\frac{1}{0.0389\ \frac{sec}{\mu M}}=25.7\ \frac{\mu M}{sec}$$

$$K_M=6.1581\ sec*25.7\ \frac{\mu M}{sec}=158\ \mu M$$

$$k_{cat}=\frac{25.7\ \frac{\mu M}{sec}}{0.142\ \mu M}=181\ s^{-1}$$

$$\frac{k_{cat}}{K_M}=\frac{181\ s^{-1}}{158\ \mu M}=1.1*10^6\ M^{-1}s^{-1}$$

Steady-state parameters for NdCld E210A, NdCld K141E and NdCld wt at pH 7.0 (50 mM potassium phosphate buffer) were not measured in this thesis, but used for comparative purposes (see Table 4.1 and Table 4.2).

k_{cat} of both mutants decreased with increasing pH which is consistent with already published data of NdCld wt (see Table 4.1) [18]. K_M varies between 121 µM and 382 µM for E210A and between 41 µM and 70 µM for K141E. The turnover number decreased in both, E210A and K141E, but not very pronouncedly in the latter. The catalytic efficiency decreased with increasing pH in NdCld wt as a result of enzymatic turnover inhibition, which seems to be also true for its mutants E210A and K141E.

It was shown that K_M of E210A was about 5-fold higher compared to wt at pH 7.0 which reflects a significant decrease in chlorite degradation. K141E exhibited wt-like behavior (see Table 4.1 and Table 4.2). At pH 5.5, which is the optimum for NdCld and its mutants, E210A showed very similar steady-state parameters compared to NdCld wt at this pH while K141E showed minor differences, such as a lower K_M and k_{cat} [18]. This points out that, in E210A, disruption in the H-bonding network between H160, E210 and K141 is more pronounced at neutral pH compared to pH 5.5 while it is subtle in K141E.

Table 4.1: Steady-state kinetics of NdCld mutants.

NdCld E210A			
pH	5.5	7.0 [9]	9.0
V_{max}	26 ± 1.0 µM/sec	-	3 ± 0.3 µM/sec
K_M	158 ± 26 µM	382 µM	121 ± 53 µM
k_{cat}	181 ± 7 s^{-1}	46.7 s^{-1}	23 ± 2 s^{-1}
k_{cat}/K_M	(1.1 ± 0.1)E+06 $M^{-1}s^{-1}$	1.2E+05 $M^{-1}s^{-1}$	(1.9 ± 0.5)E+05 $M^{-1}s^{-1}$
NdCld K141E			
pH	5.5	7.0 [9]	9.0
V_{max}	9 ± 0.2 µM/sec	-	3 ± 0.1 µM/sec
K_M	69 ± 12 µM	70 µM	41 ± 10 µM
k_{cat}	107 ± 3 s^{-1}	33 s^{-1}	28 ± 1 s^{-1}
k_{cat}/K_M	(1.6 ± 0.2)E+06 $M^{-1}s^{-1}$	4.6E+05 $M^{-1}s^{-1}$	(6.9 ± 1.2)E+05 $M^{-1}s^{-1}$

Table 4.2: Steady-state kinetics of NdCld wt.

NdCld wt	
pH	7.0 [5,9,18]
V_{max}	-
K_M	69 µM
k_{cat}	43 s^{-1}
k_{cat}/K_M	(5.9-6.2)E+05 $M^{-1}s^{-1}$

4.2.2 Electronic circular dichroism spectroscopy

4.2.2.1 NdCld

eCD is able to reveal differences in secondary and tertiary structure so it is possible to demonstrate if the mutation at E210 and K141 in NdCld change the overall fold. Moreover, thermal stability can be probed by following thermal un- and refolding, which was done for LmCld. This was done by recording a temperature curve at different pHs. Alpha helices show minima at 208 nm and 222 nm and beta sheets around 213 nm [39]. General comparison of all spectra at pH 5.5 (see bottom right of Figure 4.5) shows slightly distinct differences between NdCld wt compared to NdCld E210A, but almost no differences when compared to NdCld K141E. This can be due to structural rearrangement or different concentrations of enzyme when starting the measurement. According to the CDNN algorithm [21] secondary structures have not changed significantly, concluding that the point mutations do not affect secondary structure.

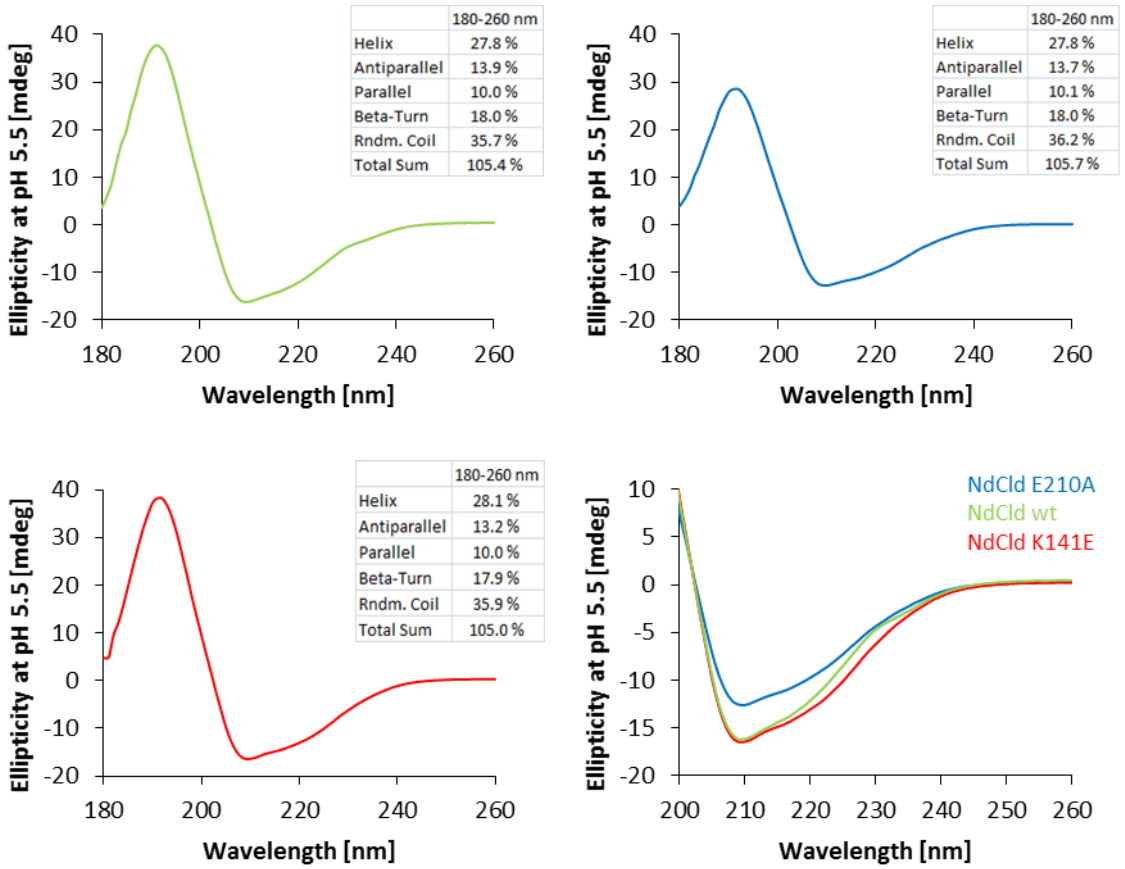

Figure 4.5: Far-UV spectra of NdCld wt (top left), NdCld E210A (top right), NdCld K141E (bottom left) at pH 5.5. Overlay of all spectra (bottom right). Diagrams include the output of CDNN [21].

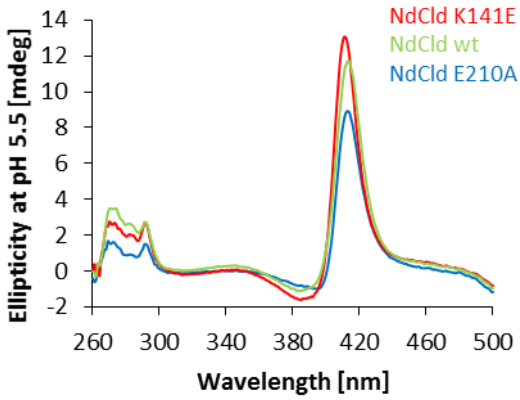

Figure 4.6: Near UV and UV-vis eCD spectra of NdCld wt (light green), E210A (blue) and K141E (red) at pH 5.5.

Heme groups usually show a signal at around 410 nm [39]. For NdCld and its mutants the Soret region gives positive ellipticity between 411 nm and 413 nm (see Figure 4.6) while aromatic amino acids are represented by the region between 260 nm and 320 nm [39].

4.2.2.2 LmCld

LmCld shows a broad transition upon heating which results in almost no ellipticity at 80°C (see top left of Figure 4.7). At 208 nm, LmCld shows an approximate transition point of 60°C at pH 4.0 while spectra of LmCld at pH 7.0 and pH 10.0 have transitition points of 47°C and 46°C, respectively. Conversely, transition midpoints have previously been reported to be 35°C for all probed pHs at 222 nm [11]. The overall stability of holo-LmCld was found to be high between pH 7.0 and pH 10.0 while at acidic conditions the protein precipitates and looses its Soret band absorbance [11].

At 20°C, the ellipticity of LmCld shows weaker signals at pH 4 and pH 10 compared to pH 7 (see top right of Figure 4.7). At neutral pH LmCld rougly consists out of 30% alpha-helices and 20% beta-sheets (see middle left of Figure 4.7). At both pH 4 and pH 10 the amount of helices decreases while the amount of sheets increases. It is noteworthy to mention that these changes are more pronounced at acidic conditions, probably due to acidic denaturation.

Middle right of Figure 4.7 shows the refolding process at pH 7. LmCld looses a large amount of ellipticity when heated to 95°C. However, after cooling down, significant ellipticity remained (approximately 50%). The same is true for pH 10.0 (see bottom right of Figure 4.7). At pH 4 LmCld also looses a large amount of ellipiticity at 95°C with little or no refolding at all (see bottom left of Figure 4.7).

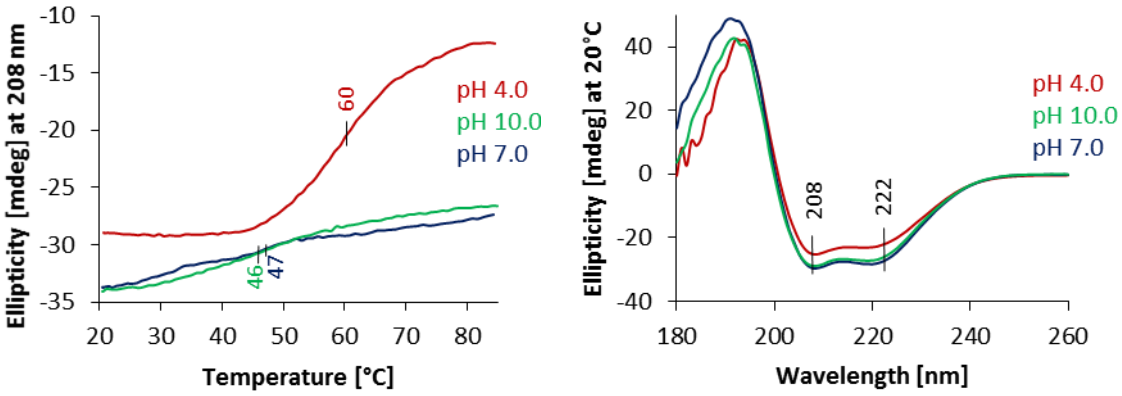

pH 4.0

	180-260 nm
Helix	27,30%
Antiparallel	15,60%
Parallel	9,90%
Beta-Turn	18,50%
Rndm. Coil	34,60%
Total Sum	105,90%

pH 10.0

	180-260 nm
Helix	28,60%
Antiparallel	14,70%
Parallel	9,30%
Beta-Turn	18,30%
Rndm. Coil	32,20%
Total Sum	103,00%

pH 7.0

	180-260 nm
Helix	30,70%
Antiparallel	11,80%
Parallel	8,80%
Beta-Turn	17,70%
Rndm. Coil	31,70%
Total Sum	100,70%

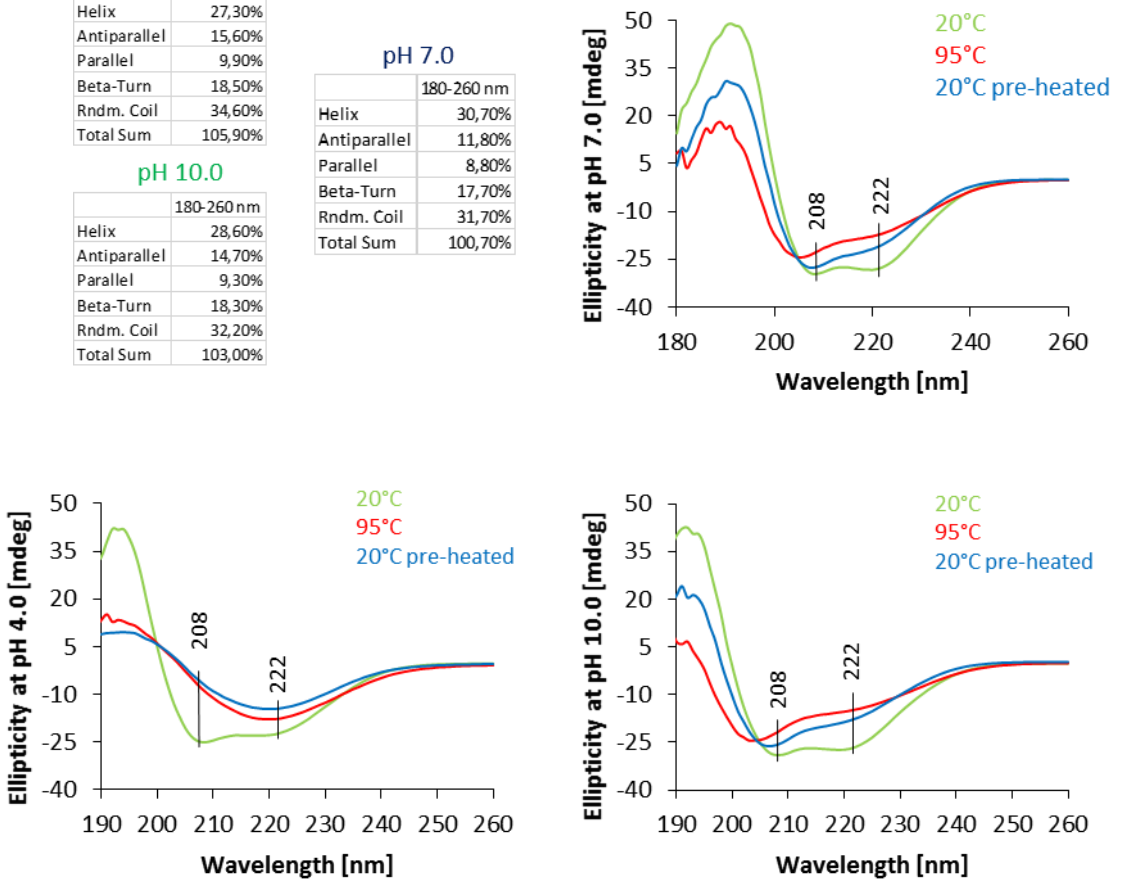

Figure 4.7: Temperature curve of LmCld at pH 4.0 (dark red), pH 7.0 (green) and pH 10.0 (dark blue) at 208 nm (top left). Overlay of all spectra at pH 4.0 (dark red), pH 7.0 (green) and pH 10.0 (dark blue) at 20°C (top right). Output of CDNN at different pHs and 20°C (middle left). Ellipticity at 20°C (light green), 95°C (red) and 20°C after cooldown (blue) at pH 7.0 (middle right), at pH 4.0 (bottom left) and pH 10.0 (bottom right).

4.2.3 Chemical unfolding of CCld measured by fluorescence spectroscopy

By monitoring the fluorescence and Soret absorbance change upon adding guanidine hydrochloride it is possible to probe the conformational stability of CCld. While the increase of intrinsic fluorescence of tryptophan yields information about the denaturation process, the decrease of Soret absorbance is related to any events concerning the cofactor heme *b*.

As expected, fluorescence rises with increasing concentrations of denaturing agent, correlating with tryptophan residues becoming solvent exposed. An intermediate step can be found at around 2.5 M.

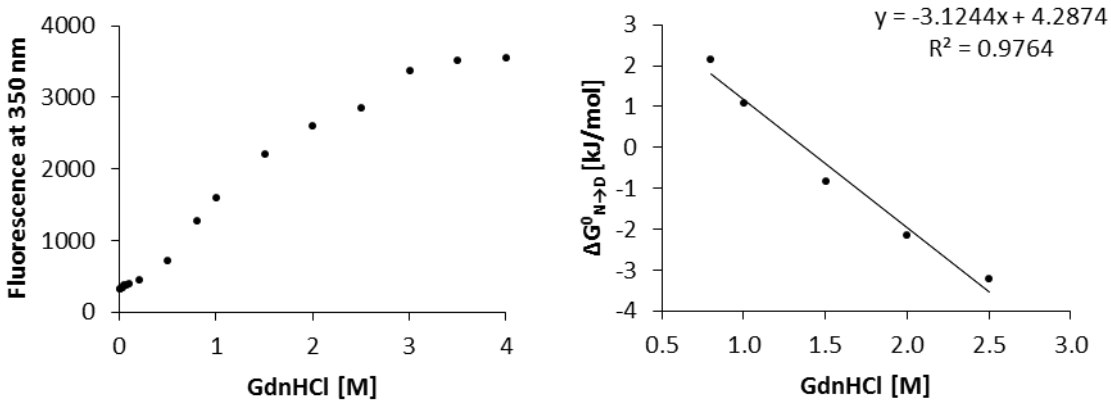

Figure 4.8: Unfolding curve: Fluorescence at 350 nm vs. GdnHCl concentration (left). Linear fit of $\Delta G^0_{N\rightarrow D}$ vs. concentration of GdnHCl (right).

Exemplary calculation:

$$\propto=\frac{(F_N-F)}{(F_N-F_D)} \quad K_{eq}=\frac{\propto}{(1-\propto)} \quad \Delta G^0_{N\rightarrow D}=-R*T*\ln K_{eq}$$

$$F_N=326.86 \quad F_D=3557.16 \quad F_{350}=725.26 \ (c_{GdnHCl}=0.5\ M)$$

$$\propto=\frac{(326.86-725.26)}{(326.86-3557.16)}=0.123$$

$$K_{eq}=\frac{0.123}{1-0.123}=0.141$$

$$\Delta G^0_{N\rightarrow D}=-8.315\ \frac{J}{mol\ K}*273{,}14K*\ln(0.141)=4.454\ \frac{kJ}{mol}$$

$\Delta G^0_{N\rightarrow D}$ is then plotted against the concentration of GdnHCl (Figure 4.8).

With increasing concentration of GdnHCl, absorbance at 407 nm decreases. This represents release of heme *b* during the unfolding process. Absorbance is completely lost at a concentration of 2.5 M in a two-state transition (see Figure 4.9).

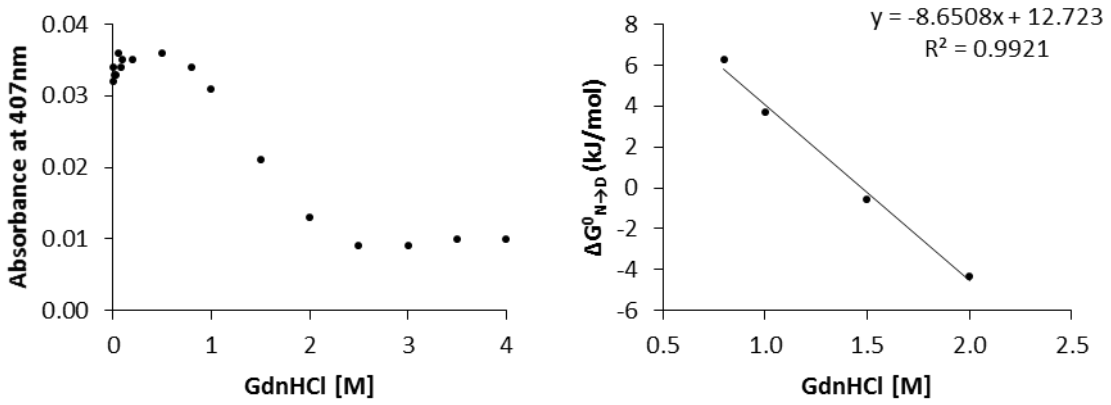

Figure 4.9: Unfolding curve: Absorbance at 407 nm vs. GdnHCl concentration (left). Linear fit of $\Delta G^0_{N\rightarrow D}$ vs. concentration of GdnHCl (right).

The following formulas were used for calculation of the absorbance unfolding parameters:

$$\propto = (A_N - A)/(A_N - A_D)$$

$$K_{eq} = \propto/(1-\propto)$$

$$\Delta G^0_{N\rightarrow D} = -R*T* \ln K_{eq}$$

$\Delta G^0_{N\rightarrow D}$ was then plotted against the concentration of GdnHCl (Figure 4.9).

Table 4.3: Unfolding parameters.

CCId		
	Fluorescence	Absorbance
pH	7.0	7.0
m-value	-3.1 ± 0.3 kJ*mol^{-1}*M^{-1}	-8.7 ± 0.5 kJ*mol^{-1}*M^{-1}
ΔG_{H_2O}	4.3 ± 0.5 kJ*mol^{-1}	12.7 ± 0.8 kJ*mol^{-1}
c_M	1.3 M	1.5 M

Calculated ΔG_{H_2O} - values indicate that heme *b* is released after complete unfolding of the protein. In comparison, the prosthetic group in pentameric NdCld is released before the protein is completely unfolded [40]. Also, CCld unfolds in a non-two-state transition. These findings suggest that the native state is followed by a heme-bound intermediate which is followed by a heme-free denatured state.

Moreover, the conformational stability of CCld was calculated to be 4.3 kJ*mol^{-1}, which is about one fourth of the value of NdCld (16.3 kJ*mol^{-1}) [40]. The heme cavities of both proteins exhibit a similar stability (both 12.7 kJ*mol^{-1}).

4.2.4 *Pre-steady-state kinetics of LmCld titrated with cyanide determined by sequential stopped-flow spectroscopy*

Cyanide can be used as an accessibility probe for the heme cavity which was done in a sequential stopped-flow approach with LmCld.

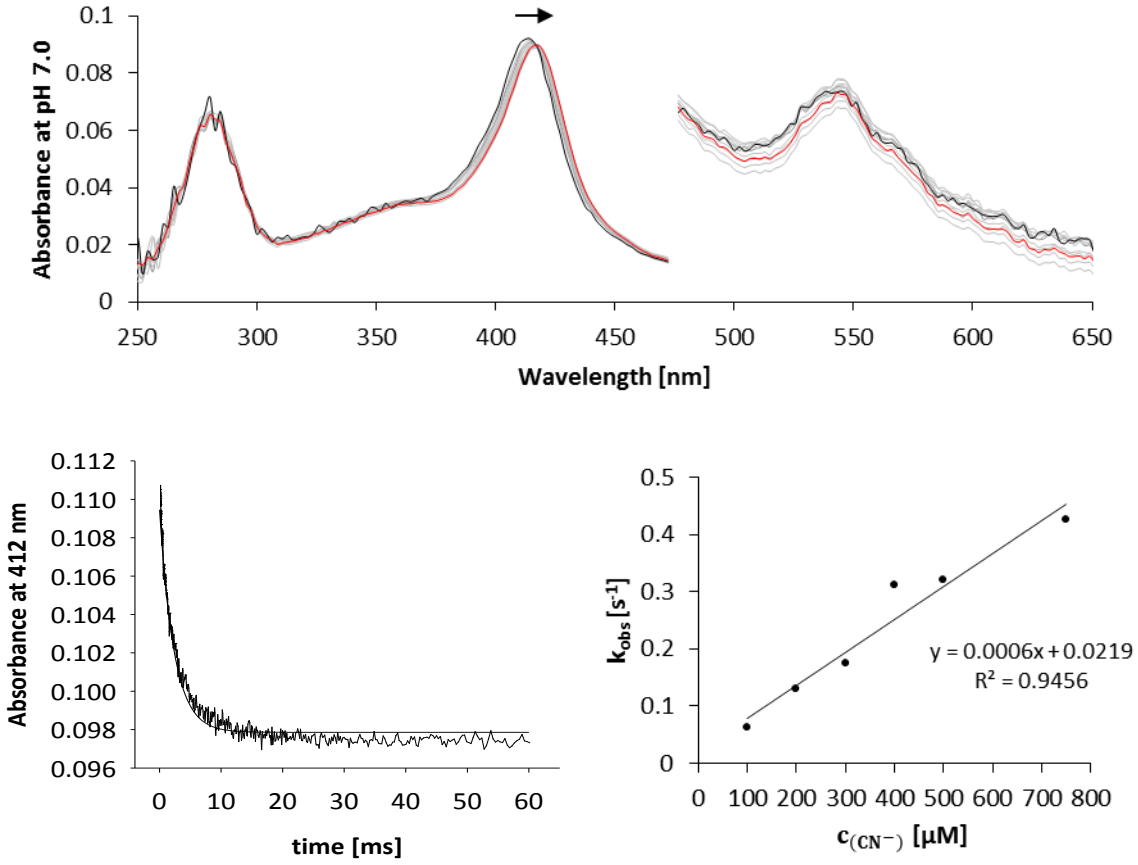

Figure 4.10: Spectral changes of LmCld upon mixing with 1000 µM cyanide at pH 7.0 (top), the first spectrum is depicted in black, the last one in red. Time trace at 412 nm and pH 7.0 (bottom left). Linear fit of k_{obs} vs. $c_{(CN^-)}$ (bottom right).

In the resting state, LmCld shows a Soret maximum at 412 nm and two Q-bands at 542 nm and 566 nm which is indicative of a low-spin system [41]. After replacing an eventual ligand, a cyanide complex is created and the Soret maximum shifts to 418 nm. Similar observations were also reported previously [11]. Calculated rate and equilibrium binding constants can be found in Table 4.4.

Table 4.4: Rate and equilibrium cyanide-binding constants of LmCld at pH 7.0.

	LmCld	NdCld [11]	NdCld E210A [9]
pH	7.0	7.0	7.0
k_{on}	600 ± 70 $M^{-1}*s^{-1}$	2.57E+06 $M^{-1}*s^{-1}$	40 $M^{-1}*s^{-1}$
k_{off}	0.022 ± 0.030 s^{-1}	9.3 s^{-1}	0.7 s^{-1}
K_D	36.5 µM	3.6 µM	17300 µM

The association rate constant of cyanide is rather low. in comparison to NdCld, k_{on} is 4300-fold lower and K_D 10-fold higher [8]. This may be due to limited accessibility of the ligand to the active site. Accessibility calculations of the LmCld crystal structure strengthen this assumption [11]. As expected, the association rate constant of NdCld E210A, which mimics the proximal architecture of LmCld, stays within one order of magnitude compared to LmCld [9,10]. However, there is a big difference between both equilibrium binding constants K_D (480-fold) [9] which is probably due to the low coefficient of determination of the linear fit (see bottom right Figure 4.10) and, with that, k_{off} and its very high standard deviation.

4.2.5 Titration of CCld and NdCld with potential ligands using UV-vis spectroscopy

By titrating CCld and NdCld with certain ligands it is possible to study the behavior and possible change of iron spin states. Moreover, respective equilibrium binding constants K_Ds can be calculated which represent the affinity of the ligand for the enzyme. Possible changes upon ligand binding on the distal and proximal side of the heme cavity can then be studied with the help of a structural approach, in which CCld in complex with fluoride and thiocyanate, respectively, was crystallized.

4.2.5.1 CCld

When titrated with fluoride, the Soret peak is slightly blue-shifted and exhibits hyperchromicity. Furthermore, upon fluoride binding, a fluoride sensitive band arises at 612 nm (see top left and right of Figure 4.11). CCld titrated with nitrite shows a slight redshift of its Soret peak (405 nm to 410 nm) at both pH values studied (i.e. pH 5.5 and 7.0). Q_v at 500 nm shifts to 540 nm with a shoulder around 570-575 nm and CT1 at 635 nm starts to disappear which reflects the spectral behavior of CCld in the presence of a low-spin ligand (see top left and right of Figure 4.12). CCld titrated with thiocyanate shows a similar behavior (see top left and right of Figure 4.13). K_D values were calculated using fitted reaction curves described by the equation y=ax/(b+x) (rectangular hyperbola) at distinct wavelengths. Fluoride binding was followed at 612 nm, nitrite binding at 570 nm (pH 5.5) and 575 nm (pH 7.0) and thiocyanate binding at 575 nm (see bottom left and right of Figure 4.11, Figure 4.12 and Figure 4.13, respectively).

Fluoride:

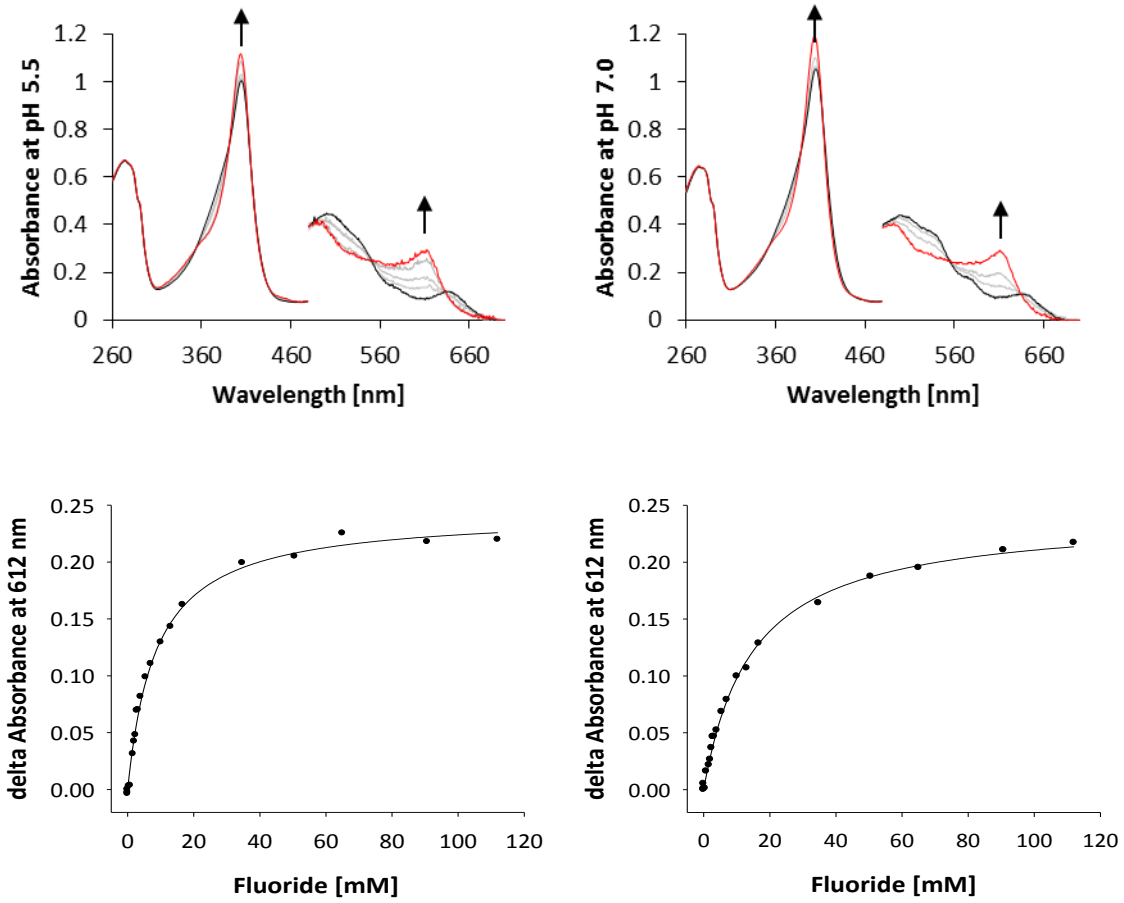

Figure 4.11: Titration of CCld with fluoride at pH 5.5 (top left) and pH 7.0 (top right). The first recorded spectrum (i.e. CCld without ligand) is depicted in black, the last one (i.e. CCld supplemented with 112 mM fluoride) in red. Absorbance at 612 nm vs. fluoride concentration at pH 5.5 (bottom left). Absorbance at 612 nm vs. fluoride concentration at pH 7.0 (bottom right). Data points were fitted with a rectangular hyperbolic function.

Nitrite:

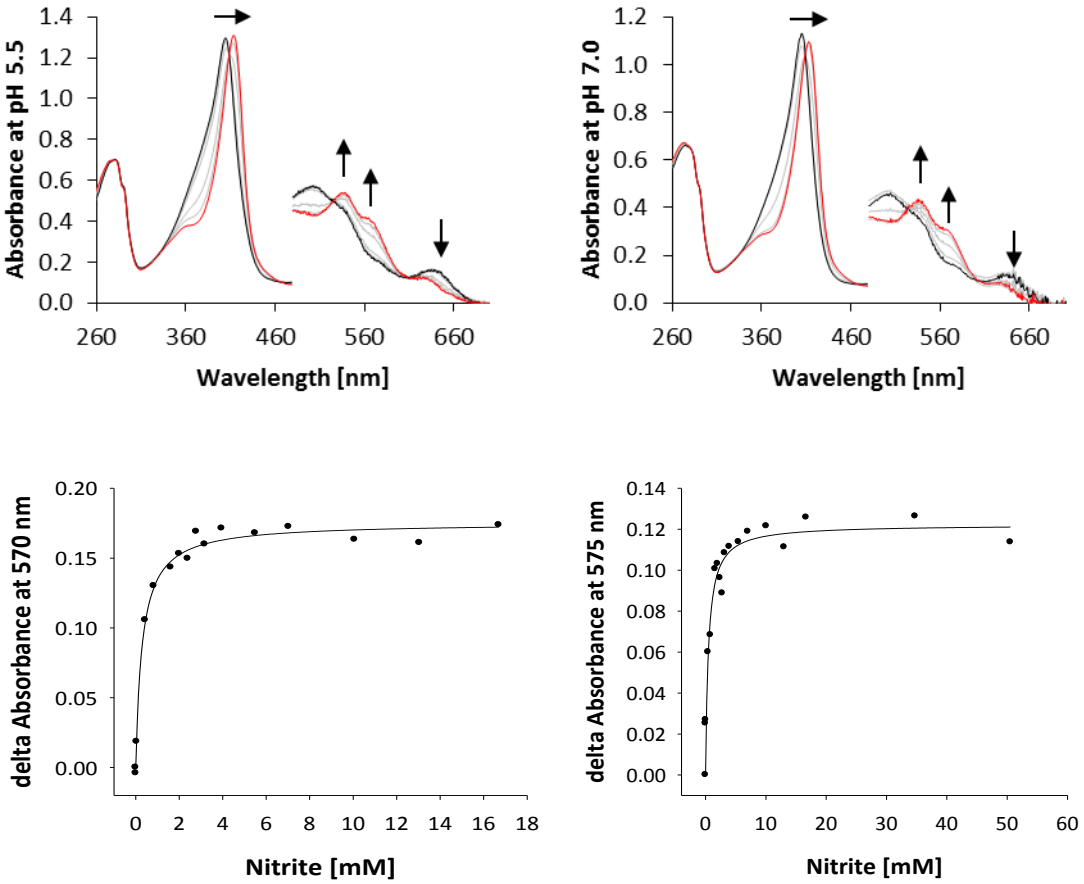

Figure 4.12: Titration of CCId with nitrite at pH 5.5 (top left) and pH 7.0 (top right). The first recorded spectrum (i.e. CCId without ligand) is depicted in black, the last one (i.e. CCId with 16.7 and 50.56 mM nitrite, respectively) in red. Absorbance at 570 nm vs. nitrite concentration at pH 5.5 (bottom left). Absorbance at 575 nm vs. nitrite concentration at pH 7.0 (bottom right). Data points were fitted with a rectangular hyperbolic function.

Thiocyanate:

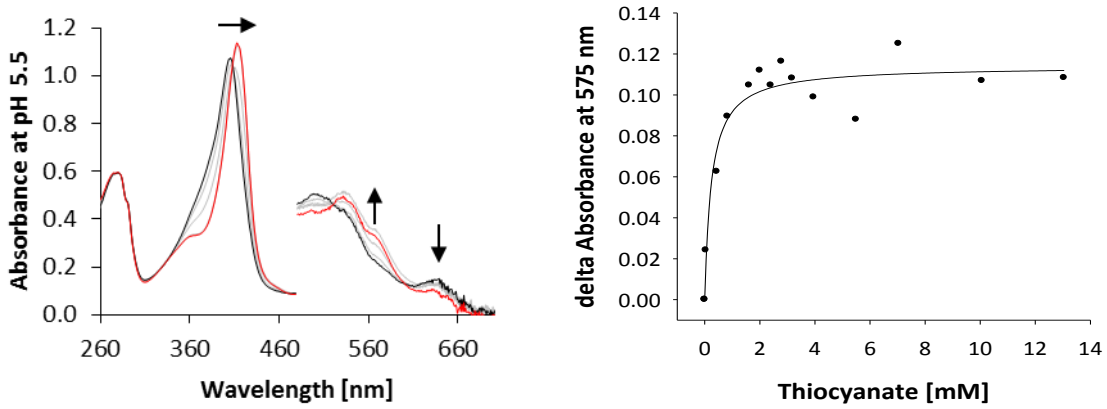

Figure 4.13: Titration of CCld with thiocyanate at pH 5.5 (left). The first recorded spectrum (i.e. CCld without ligand) is depicted in black, the last one (i.e. CCld with 16.7 mM thiocyanate) in red. Absorbance at 575 nm vs. thiocyanate concentration at pH 5.5 (right). Data points were fitted with a rectangular hyperbolic function.

4.2.5.2 NdCld

The Soret maximum of NdCld shifts from 408 nm to 404 nm at pH 5.5 and from 410 nm to 405 nm at pH 7.0. Moreover, the fluoride-sensitive band at 612 nm appears (see top left and right of Figure 4.14). This behavior is similar to CCld titrated with fluoride. NdCld titrated with nitrite shows a redshift of the Soret peak from 407 nm to 410 nm at pH 5.5 and from 409 nm to 410 nm at pH 7.0. Q_v at around 515 nm shifts to 540 nm with a shoulder around 565 nm at pH 5.5. At pH 7.0, Q_v shifts from 525 nm to 538 nm with a shoulder around 565 nm (see top left and right of Figure 4.15). When titrated with thiocyanate, the Soret band at 409 nm shifts to 357 nm. It is difficult to reliably determine the proper spin state because absorbance is largely lost in the region between 460 nm and 660 nm (see top left and right of Figure 4.16). K_D values were calculated using fitted reaction curves described by the equation y=ax/(b+x) (rectangular hyperbola) at a distinct wavelength. Fluoride was followed at 612 nm, nitrite at 370 nm and thiocyanate at 411 nm (see bottom left and right of Figure 4.14, Figure 4.15 and Figure 4.16). It was not possible to determine an appropriate fit for NdCld titrated with nitrite at pH 5.5. Thus, no K_D could be calculated.

Fluoride:

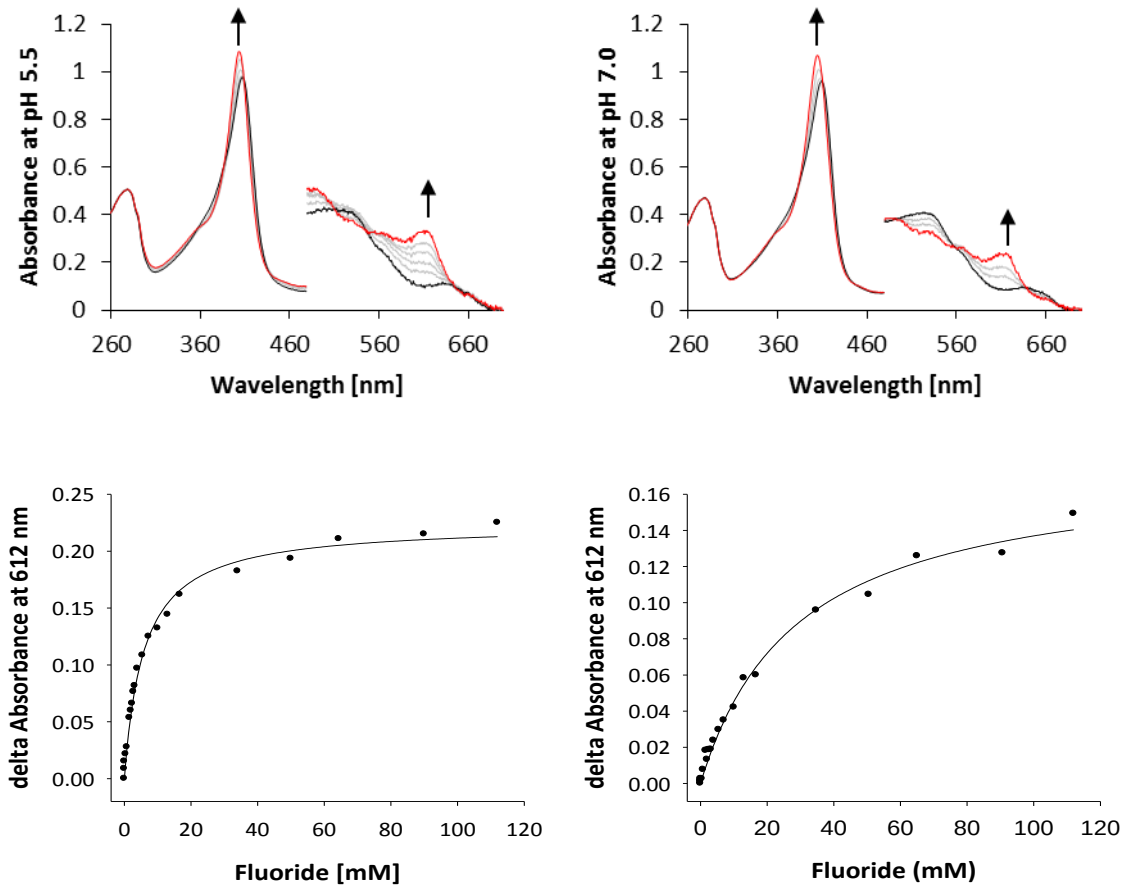

Figure 4.14: Titration of NdCld with fluoride at pH 5.5 (top left) and pH 7.0 (top right). The first recorded spectrum (i.e. NdCld without ligand) is depicted in black, the last one (i.e. NdCld with 112 mM fluoride) in red. Absorbance at 612 nm vs. fluoride concentration at pH 5.5 (bottom left). Absorbance at 612 nm vs. fluoride concentration at pH 7.0 (bottom right). Data points were fitted with a rectangular hyperbolic function.

Nitrite:

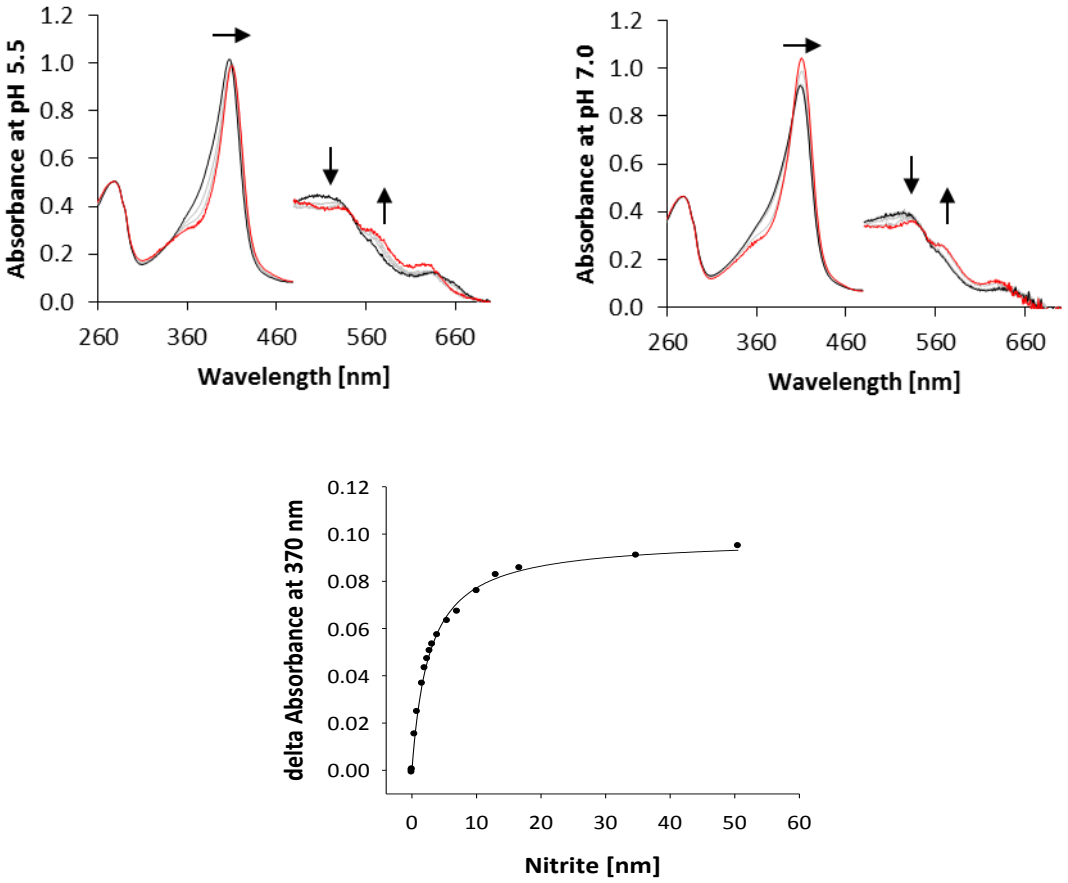

Figure 4.15: Titration of NdCld with nitrite at pH 5.5 (top left) and pH 7.0 (top right). The first recorded spectrum (i.e. NdCld without ligand) is depicted in black, the last one (i.e. NdCld with 50.56 mM nitrite) in red. Absorbance at 370 nm vs. nitrite concentration at pH 7.0 (bottom). Data points were fitted with a rectangular hyperbolic function.

Thiocyanate:

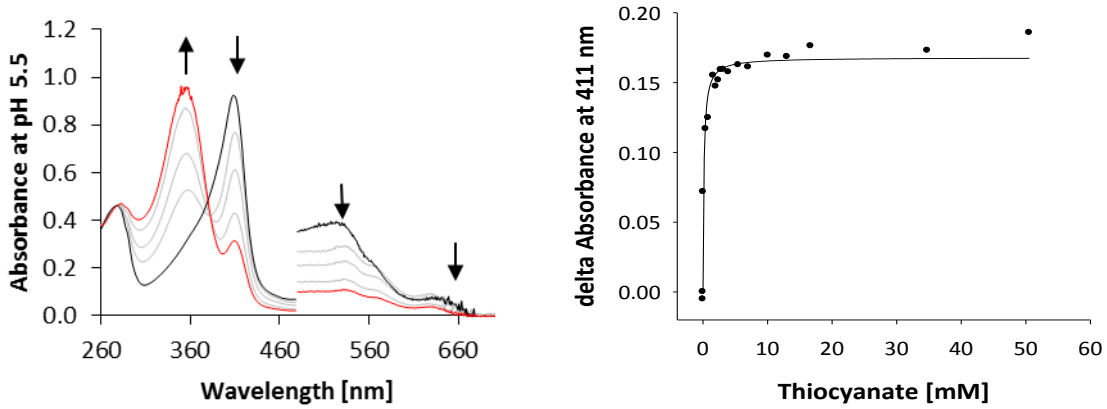

Figure 4.16: Titration of NdCld with thiocyanate at pH 5.5 (left). The first recorded spectrum (i.e. NdCld without ligand) is depicted in black, the last one (i.e. NdCld with 50.56 mM thiocyanate) in red. Inverted absorbance at 411 nm vs. thiocyanate concentration at pH 5.5 (right). Data points were fitted with a rectangular hyperbolic function.

4.2.5.3 Comparison of equilibrium binding constants

Table 4.5: K_D values for CCld titrated with different ligands.

CCld		
pH	5.5	7.0
Fluoride	8.6 ± 0.51 mM	14.7 ± 0.58 mM
Nitrite	0.3 ± 0.02 mM	0.5 ± 0.11 mM
Thiocyanate	0.2 ± 0.08 mM	-

For CCld, K_D values for fluoride are 10-fold greater compared to nitrite and thiocyanate, reflecting a lower affinity of the former to the enzyme. Principally, K_D values of all mentioned ligands rise with increasing pH indicating a decrease of affinity.

Table 4.6: K_D values for NdCld titrated with different ligands.

NdCld		
pH	5.5	7.0
Fluoride	5.9 ± 0.36 mM	29.1 ± 2.54 mM
Nitrite	no appropriate fit	2.7 ± 0.10 mM
Thiocyanate	0.1 ± 0.04 mM	-

In NdCld, the K_D for fluoride at pH 7.0 is 10-fold greater compared to nitrite, which is a similar behavior as of CCld. K_D for thiocyanate is similar to K_D for CCld.

To sum up, fluoride acts as a high-spin ligand for both enzymes. Nitrite is a low-spin ligand for both, CCld and NdCld, but it should be noted that the spectral shifts upon addition of nitrite are less distinct in the latter. Thiocyanate shows the characteristics of a low-spin ligand for CCld whereas for NdCld the spin state could not be determined.

4.3 Structural studies

4.3.1 Introduction

Overexpression of CCld in *E. coli* yielded sufficient amounts of protein for crystallization trials. For this master thesis, native CCld but also CCld in complex with fluoride and thiocyanate were crystallized to determine and compare their three-dimensional structures. Fluoride and thiocyanate cause distinct spectral features when coordinated with heme *b* (as high-spin- and low-spin ligand, respectively) and may result in rearrangement of specific residues in the protein or, more specifically, the active site. Differences can be visualized by generating overlays using the molecular visualization program Pymol [42].

After close inspection of the electron density map of the native structure, a ring-like positive electron density could be found near the iron on the distal site in the difference density map which is believed to be imidazole. A contamination with the aromatic heterocycle may have happened because of an insufficient clean-in-place procedure (CIP) of the SEC system in a previous run. The dataset of CCld in complex with fluoride is not shown because an insufficient amount of fluoride was used during crystal soaking. However, an in-house dataset was used for the generation of anomalous maps.

Both, CCld in complex with imidazole and thiocyanate crystallized in the *P*1 space group with a maximum resolution of 1.1 Å and 1.08 Å, respectively.

4.3.2 Crystallization conditions

The following section describes the optimizing process of the crystallizing conditions of all shown structures. Initial screens were done using the commercial screens JCSG-plus™ and PEGRx. Two of the JCSG-conditions (see Table 4.7) yielded well-shaped crystals and one of them diffracted in a resolution range of 1.139 - 1.1 Å in the highest resolution shell (see Table 4.9). To further optimize the crystallizing conditions in general, a series of subsequent individual optimization screens were designed which, at the end, increased the overall quality of crystal shapes and diffraction patterns.

Init-Screen

The Init-Screen (see Supplementary Figure 6.1) was designed based on the information gained from the commercial screens. Several salts, buffers and crystallizing agents were used in different concentrations. The pH was increased in increments of 0.5 from pH 5.5 to pH 7.0.

Opt2- and Opt3-Screen

MES and $MgSO_4$ proved to be useful in the commercial screens and the Init-screen, so they were used to design further optimized screens (see Supplementary Figure 6.2 and Supplementary Figure 6.3). Polyethylene glycol (PEG) and glycerol also improved crystal growth of CCld. pH 5.5 did not yield notable crystals in the Init-screen, so only pH 6.0, pH 6.5 and pH 7.0 were used in this approach. In D2, F10 (Opt2) and F7 (Opt3) moderately sized crystals grew (see Table 4.7). Already optimized conditions of Opt2 and Opt3 were then used to set up 24-well Linbro plates.

Table 4.7: 96-well plates with notable crystallizing conditions.

Name of screen	Type (well)	Technique	Condition	Cryoprotectant
JCSG	Commercial (G5.2)	Sitting-drop	0.005 M $CoCl_2$, 0.005 M $CdCl_2$, 0.005 M $MgCl_2$, 0.005 M $NiCl_2$, 0.005 M HEPES pH 7.5, 12% PEG 3350	25% 2-Methyl-2,4-pentanediol (MPD)
JCSG	Commercial (E9)		0.1 M MES pH 6.5, 1.6 M $MgSO_4$	25% MPD
Opt2	Individual (D2)		0.09 M $MgSO_4$, 22% PEG 3350, 0.1 M MES pH 6.5	25% MPD
Opt2	Individual (F10)		1.45 M $MgSO_4$, 0.1 M MES pH 6.5, 5% Glycerol	25% Glycerol
Opt3	Individual (F7)		1.53 M $MgSO_4$, 0.1 M MES pH 6.5, 5% Glycerol	25% Glycerol
Opt3	Individual (F7)		1.53 M $MgSO_4$, 0.1 M MES pH 6.5, 5% Glycerol	25% Glycerol

To sum up, several crystallizing conditions produced well-shaped crystals which also diffracted satisfactorily. The three final structures are summarized in Table 4.8.

Table 4.8: Overview structures.

	1	2	3
Protein	CCld	CCld	CCld
Ligand	Imidazole	Fluoride	Thiocyanate
Beamline	ESRF ID23-1	in-house	ESRF ID23-1
Processed with	XDS [30]	Proteum suite	XDS [30]
Phases solved by	MR	SAD	MR
Incident wavelength	0.973 Å	1.54 Å	0.973 Å
Crystallizing condition	0.005 M $CoCl_2$, 0.005 M $CdCl_2$, 0.005 M $MgCl_2$, 0.005 M $NiCl_2$, 0.005 M HEPES pH 7.5, 12% PEG 3350	1.45 M $MgSO_4$, 0.1 M MES pH 6.5, 5% Glycerol	0.09 M $MgSO_4$, 0.1 M MES pH 6.5, 22% PEG 3350

Final refinement statistics are shown in Table 4.9 and Table 4.10 .

4.3.3 Oligomeric assembly and subunit structure

CCld was shown to be a dimer in solution [6]. It also crystallizes as a dimer (see Figure 4.17) like other clade 1 Clds such as NwCld [13]. Each subunit consists of two domains with a Ferredoxin-like fold which was also described in functional clade 1 Clds [8], functional clade 2 Clds [13] but also non-functional Clds [11]. Heme *b* can be found in each subunit in the C-terminal domain (which results in two heme *b* – molecules per molecule). The primary sequence of CCld is about 25% shorter compared to clade 1 Clds such as NdCld which is due to amino acids lacking the N-terminal domain. No disulfide bonds can be found since only one single cysteine is present. Moreover, looking at a surface representation (see Figure 4.18) the substrate channel appears to be rather broad which makes heme *b* supposedly well accessible for their substrate.

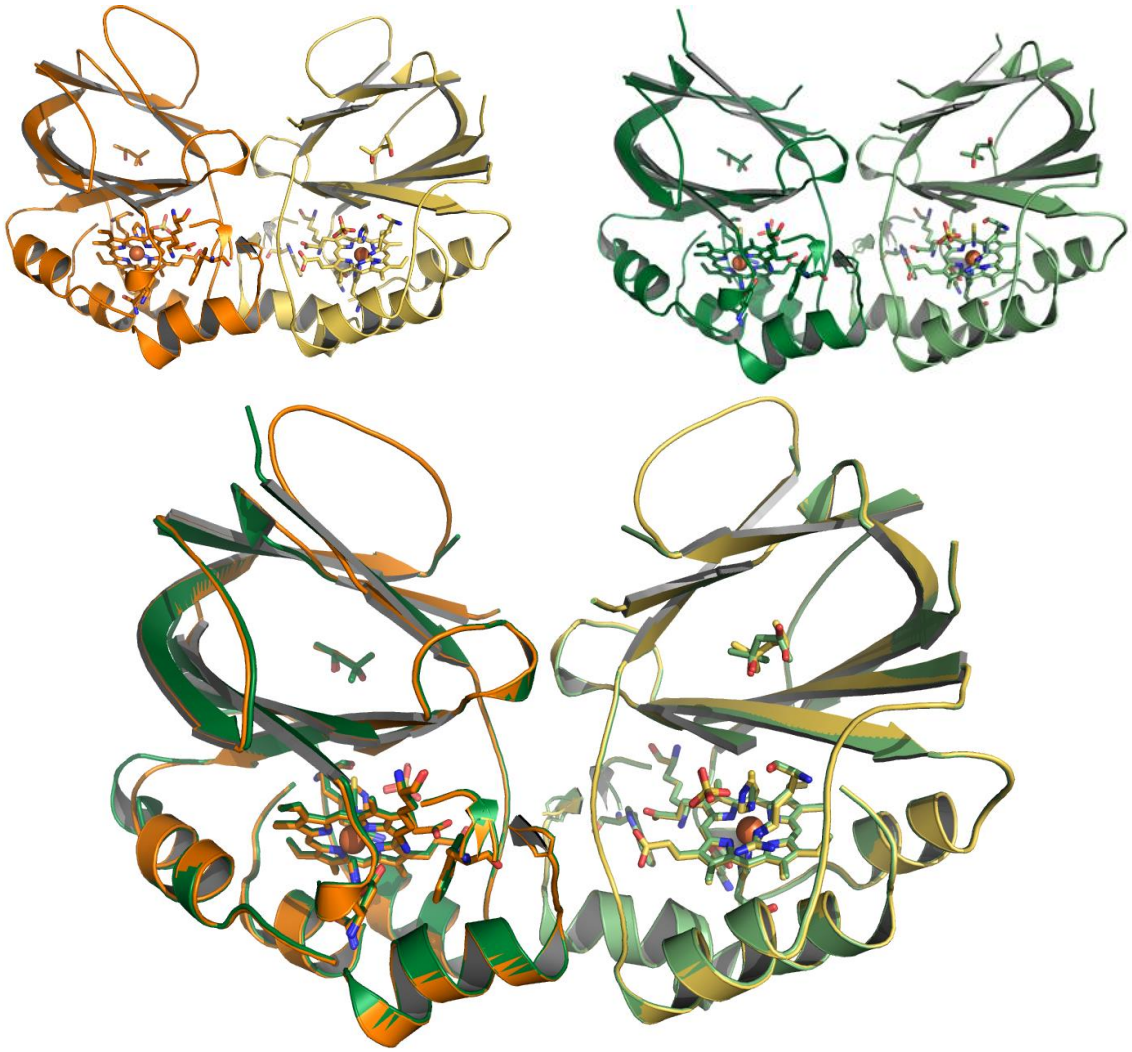

Figure 4.17: Oligomeric assembly of CCld in complex with imidazole (top left). Oligomeric assembly of CCld in complex with thiocyanate (top right). Overlay of both structures (bottom).

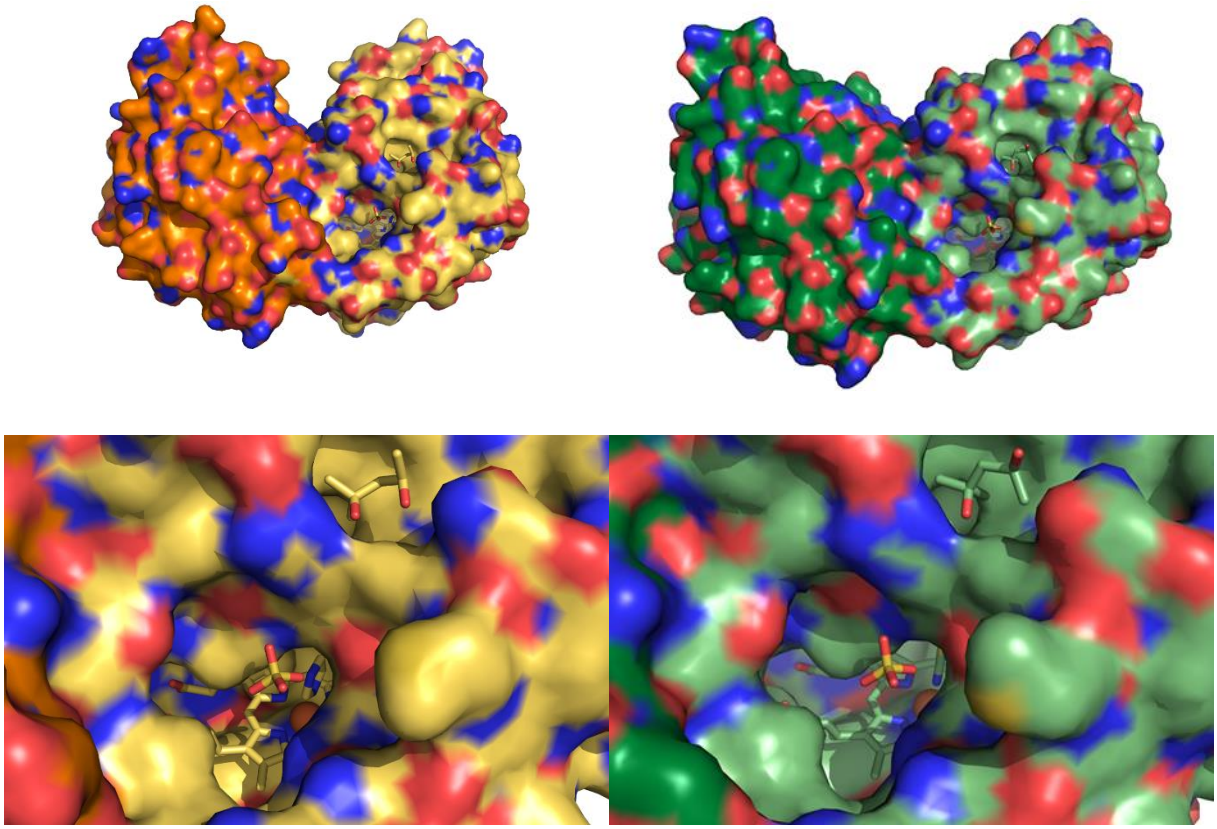

Figure 4.18: Surface representations of CCld in complex with imidazole (top left) and thiocyanate (top right) with close ups on their substrate channels (bottom left and right).

A region with the length of seven amino acids (residues 41 - 47) of CCld in complex with thiocyanate could not be modelled because of poor electron density most likely because this region is highly flexible. This results in a different surface representation compared to CCld in complex with imidazole (see Figure 4.18). The beginning and the end of the missing loop are indicated by errors in Figure 4.17.

4.3.4 Active site cavity

4.3.4.1 Proximal H-bonding system

Several conserved amino acid residues can be found at the proximal site of the heme (see Figure 4.19). H114 serves as a coordination partner of the heme iron and forms a hydrogen bond with E167 which in turn is hydrogen bonded to K92. Also, K92 is in hydrogen bonding distance to one propionate group of the heme. This conserved proximal H-bonding system which was recently described for NdCld [10] is present in all solved structures of CCld. It is reported that its disruption changes redox properties of the iron but also the behavior of bound ligands [10].

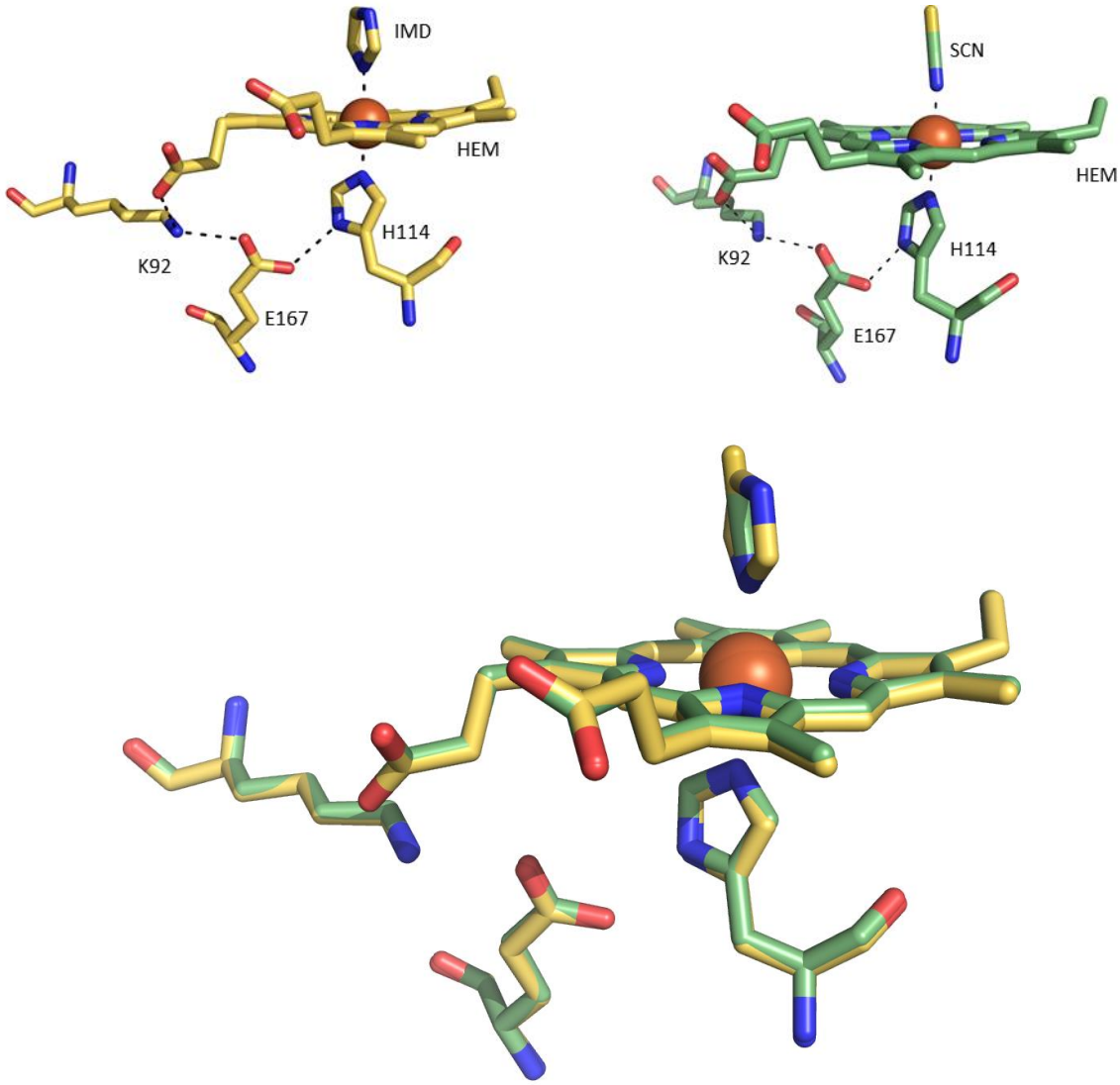

Figure 4.19: Proximal site of CCld in complex with imidazole (top left) and thiocyanate (top right). Overlay of the cavity of both structures (bottom). Assumed H-bonds on the proximal site but also interactions of heme iron with H114 and imidazol/thiocyanate are shown as dotted black lines.

Superposing CCld in complex with imidazole and thiocyanate reveals a high structural similarity, suggesting that binding of either ligand results in no notable difference of the distal and proximal architecture.

4.3.4.2 Distal site

In Figure 4.20 all distal ligands but also R127 ans Q74 are shown. The bending angle of thiocyanate was expected to be 180° since SCN shows linear geometry. However, SCN's actual bending angle is approximately 170° (see Figure 4.20). Angles of 180° are common, but also lower angles have been reported so far [43,44].

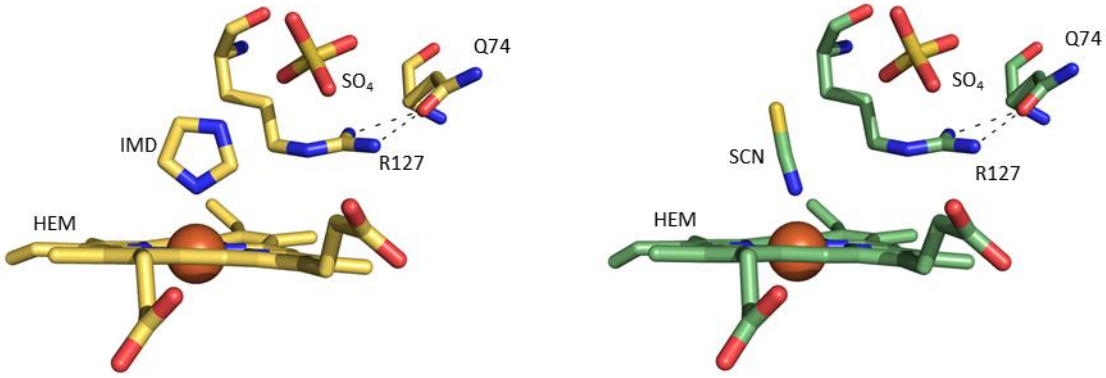

Figure 4.20: Distal site of CCld in complex with imidazole (left) and thiocyanate (right). Assumed H-bond are shown as dotted black lines.

The distal arginine R127 is supposed to play an important role in the stabilization of the substrate as well as the intermediate [5,8] and it was theorized that it prevents the reaction intermediate hypochlorite from escape in NdCld [18]. It forms hydrogen bonds with Q74.

In both structures a significant area of positive electron density is visible in the difference density map near R127. It was interpreted as sulfate in other structures, since the anion was part of buffers [8]. However, sterically it would be possible that the side chain of the distal arginine, which is supposed to be highly flexible, changes its position, thereby resulting in the above mentioned positive electron density.

To verify the presence of sulfate, an anomalous map was created with phenix.maps [25] using a fluoride dataset. Although the incident wavelength of the in-house X-ray machine (1.54 Å) is not at the absorption edge of sulfur (around 5 Å, see Figure 3.8) conclusions can be drawn because the scattering factor of sulfur is still higher compared to typical elements in biomolecules (N, O, C) [27]. In the anomalous map, a positive area of electron density appears near the side chain of the distal arginine which refutes the idea of a flipped arginine side chain but is indicative of a sulfur containing molecule at this position. It is noteworthy to mention, that in both structures the distal arginine points away from the heme iron which also was reported in other structures [8,13].

4.3.4.3 Heme planarity

Interestingly, heme *b* is not planar but clearly tilted not only in CCld in complex with imidazole but also in complex with thiocyanate (see Figure 4.21). The shift obviously originates from one of the two pyrrolic groups which contain vinyl residues.

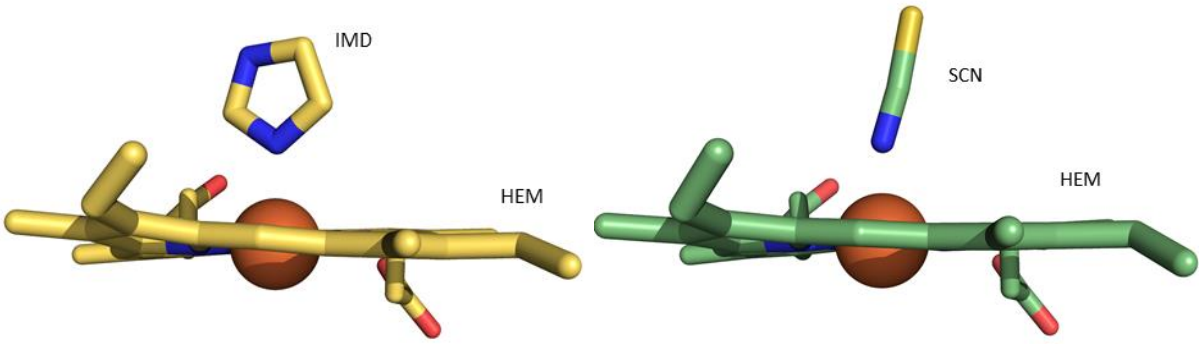

Figure 4.21: Representation of tilted heme *b* of CCld in complex with imidazole (left) and thiocyanate (right). Figures produced with Pymol [42].

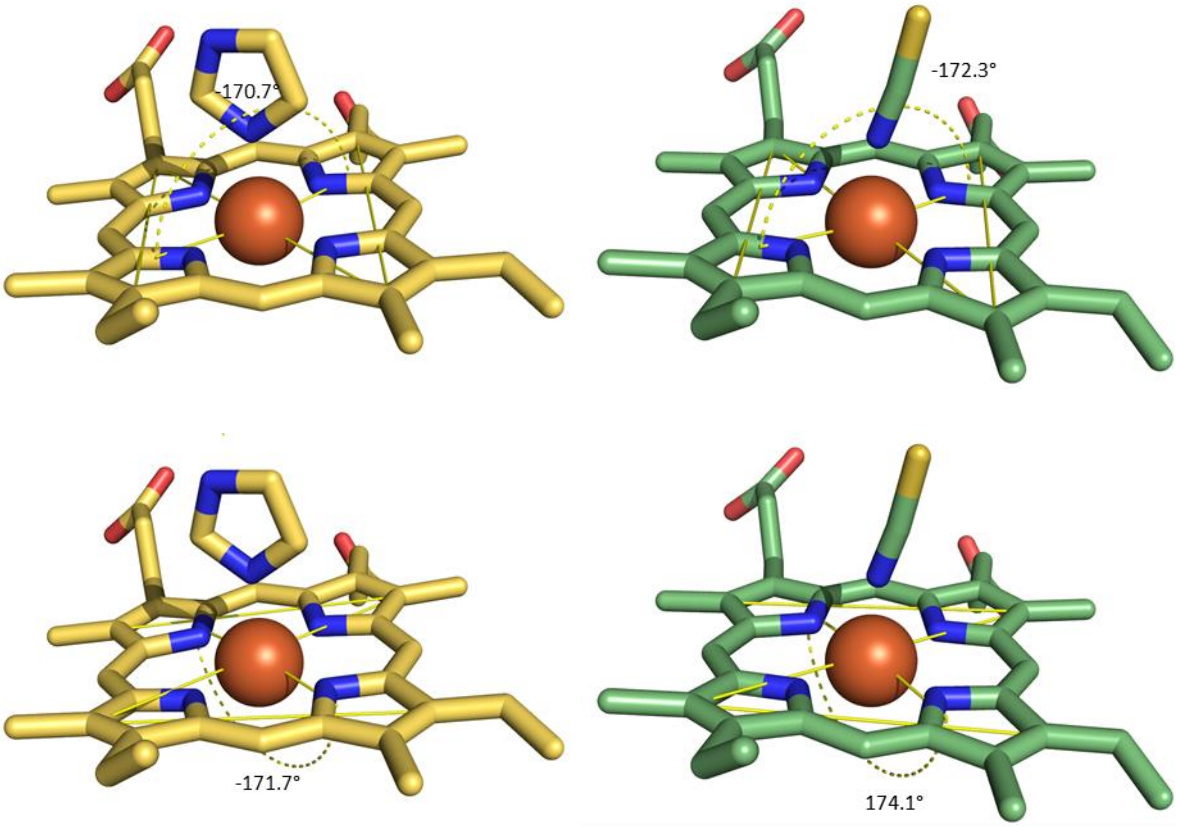

Figure 4.22: Two different approaches to calculate dihedral angles of heme *b* of CCld in complex with imidazole (top and bottom left) and CCld in complex with thiocyanate (top and bottom right).

In an approach to measure dihedral angles from different points (see Figure 4.22), angles between 171° and 172° for CCld in complex with imidazole, and between 173° and 174° for CCld in complex with thiocyanate were obtained. Dihedral angles around 180° would indicate clear planarity. Tilted heme molecules are also present in NdCld structures in complex with thiocyanate and imidazole [8,9]. Reasons

for the tilt may include the coordination process of heme iron with distal ligands, but also the presence of nearby (charged) residues.

4.3.5 MPD and ions

MPD is used as cryoprotectant for CCld crystals. In both structures, one molecule of MPD can be found in a small cavity on the surface of the protein near the entrance of the substrate channel (see Figure 4.18). In Figure 4.23, MPD and all residues within a distance of 5 Å are shown. R128 likely mediates moderate to weak electrostatic interactions with its oxygens to keep MPD in place.

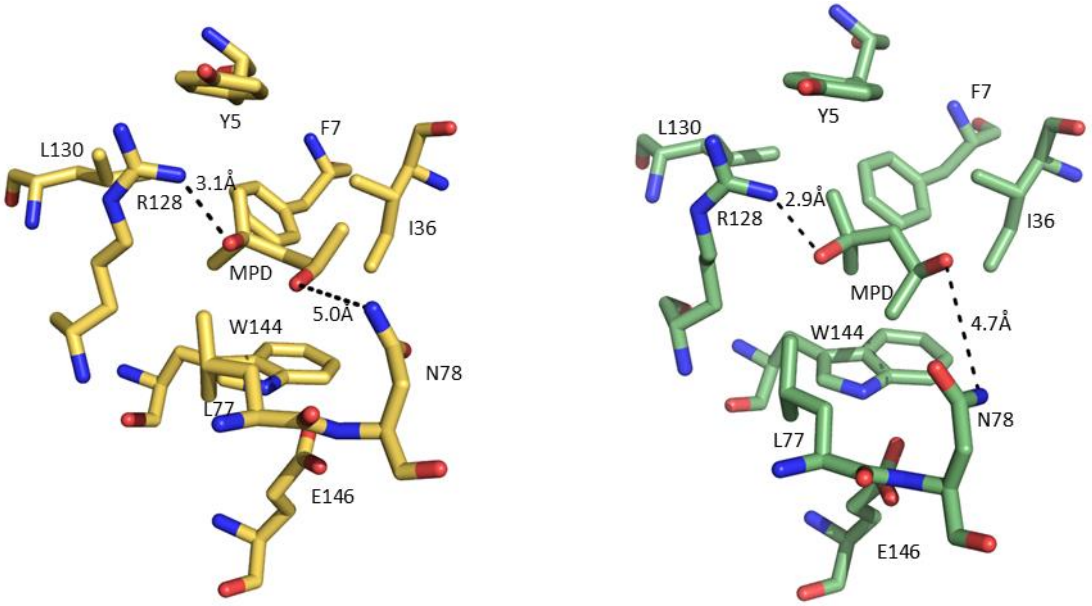

Figure 4.23: MPD and its environment of CCld in complex with imidazole (left) and thiocyanate (right). Dotted black lines show distances between depicted residues.

Generally speaking, it is difficult to reliably assign unmodelled electron density to proper ions, so it is likely that anions and cations are sometimes incorrectly replaced by water molecules [23]. By analysing the coordination sphere of relevant ions and the anomalous scattering length, it is possible to identify the actual ion. In Figure 4.24, the difference in anomalous scattering lengths between different elements is depicted. There is one very prominent area of positive electron density present in all structures near R4 of both subunits which is believed to be a negatively charged monoatomic ion binding to the positively charged side chains of R4 from both subunits. The only possible candidate is chloride, which is part of the media and reagents to adjust the pH in all investigated structures. Adding chloride to the model did not change the positive electron density significantly which is an indication that its anomalous signal is not high enough to create a density like this during the Fourier transform. This leaves the true occupation unassigned.

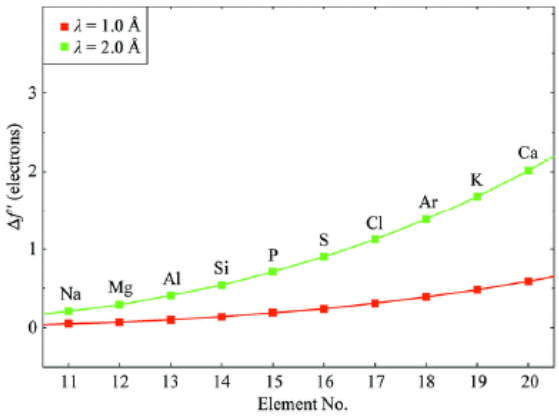

Figure 4.24: Anomalous scattering length values in number of electrons for different elements at two wavelengths [45].

4.3.6 Crystallographic parameters

4.3.6.1 CCld in complex with imidazole

Table 4.9: Crystallographic parameters of CCld in complex with imidazole.

Wavelength (Å)	0.973 Å
Resolution range (Å)	42.42 - 1.1 (1.139 - 1.1)
Space group	P 1
Unit cell (Å)	51.649 54.891 94.133 99.72 94.92 98.81
Unique reflections	381823 (35866)
Completeness (%)	0.93
Wilson B-factor	11.64
Reflections used in refinement	377991 (35457)
Reflections used for R-free	18839 (1797)
R-work	0.1734 (0.3944)
R-free	0.1978 (0.4397)
Number of non-hydrogen atoms	7369
macromolecules	6145
ligands	244
Protein residues	724
RMS (bonds)	0.022
RMS (angles)	1.21
Ramachandran favoured (%)	96
Ramachandran allowed (%)	3.2
Ramachandran outliers (%)	0.27
Rotamer outliers (%)	1.7
Clashscore	1.49
Average B-factor	21.50
macromolecules	19.74
Ligands	15.23
solvent	34.09

Statistics for the highest-resolution shell are shown in parentheses.

4.3.6.2 CCld in complex with thiocyanate

Table 4.10: Crystallographic parameters CCld in complex with thiocyanate.

Wavelength (Å)	0.973 Å
Resolution range (Å)	46.08 - 1.08 (1.119 - 1.08)
Space group	P 1
Unit cell (Å)	51.677 54.706 94.136 99.79 94.85 98.81
Unique reflections	379605 (34820)
Completeness (%)	0.88
Wilson B-factor	11.59
Reflections used in refinement	375607 (34582)
Reflections used for R-free	18608 (1761)
R-work	0.1698 (0.3991)
R-free	0.1956 (0.4299)
Number of non-hydrogen atoms	7430
macromolecules	5956
ligands	236
Protein residues	699
RMS (bonds)	0.015
RMS (angles)	1.30
Ramachandran favoured (%)	97
Ramachandran allowed (%)	2.6
Ramachandran outliers (%)	0
Rotamer outliers (%)	0.81
Clashscore	2.19
Average B-factor	20.18
macromolecules	17.74
Ligands	15.72
solvent	32.77

Statistics for the highest-resolution shell are shown in parentheses.

5 Conclusion

Chlorite dismutases were extensively examined in this thesis. While NdCld and LmCld were studied thoroughly with the help of biochemical methods, a crystallographic approach was chosen additionally for CCld. All studied Clds represented their respective clade (or non-functional Clds in the case of LmCld).

5.1 NdCld

NdCld wt and its mutants, K141E and E210A, were investigated in three different ways: their steady-state parameters were determined using a Clark-type electrode, possible differences in secondary and tertiary structure were studied in an approach which involved eCD, and their behaviour upon addition of specific ligands was examined UV-vis spectroscopically.

Both mutants of NdCld, K141E and E210A, were interesting study objects as they manipulate the proximal H-bond bonding system [9]. The determination of k_{cat} at pH 5.5 and pH 9.0 lead to the conclusion, that, like with NdCld wt, enzymatic turnover inhibition increased with pH. The affinity of the both mutant enzymes for the substrate did not change significantly while also k_{cat}/K_M stayed within one order of magnitude. It should be pointed out, however, that H-bond disruption (manifested in enzyme inactivation) in E210A is more pronounced at neutral pH compared to pH 5.5. This is due to a 5-fold higher K_M at pH 7.0, which reflects a significant decrease in chlorite degradation, and overall similar steady-state parameters at pH 5.5 when compared to wt.

The point mutations of both variants did not change secondary structure significantly.

Titration of NdCld wt with fluoride at both pH values studied (i.e. pH 5.5 and 7.0) exhibited hyperchromicity of the Soret peak, and the generation of a fluoride sensitive band at 612 nm was observed. Titration with nitrite showed a redshift of Q_v but no clear conclusion could be drawn regarding its spin state. Calculated K_D values for fluoride are 10-fold greater compared to nitrite, reflecting a lower affinity of the former to the enzyme.

5.2 LmCld

To determine the thermal stability of LmCld, its thermal un- and refolding was investigated with an eCD spectrophotometer at pH 4.0, pH 7.0 and pH 10.0. Moreover, the heme cavity architecture was examined by using cyanide as an accessibility probe in a sequential stopped-flow approach.

The eCD spectrum of LmCld at 208 nm shows a different behaviour at pH 4.0 compared to pH 7.0 and pH 10.0 which represents notable differences in the secondary structure. At pH 4.0, LmCld looses its ellipticity at the end of a broad transition range and there is little or no refolding at all. These are indications for acidic denaturation, but, conversely, LmClds calculated transition point is notably higher (60°C) than previously reported (35°C) at pH 4.0 [11]. At 20°C, LmCld exhibits a stronger signal at pH 7.0 compared to pH 4.0 and pH 10.0 over the examined wavelength range. Also, it remains 50% of its ellipticity after cooling down.

Interpretation of rate and equilibrium binding constants but also accessibility calculations led to the assumption, that cyanide has a limited accessibility to the active site of LmCld. This may be due to a flexible stretch of amino acids which is positioned in front of the binding site [11]. Moreover, the cyanide association rate constant stays within one order of magnitude compared to NdCld E210A, which mimics the proximal architecture of LmCld. Calculated equilibrium binding constants were difficult to interpret because of the elevated standard deviation of $k_{off.}$

5.3 CCld

CCld was investigated by probing its conformational stability using fluorescence spectroscopy. Also, its behaviour upon addition of ligands was determined UV-vis spectroscopically. This was followed by a structural approach, in which the three-dimensional structure of CCld in complex with imidazole as well as thiocyanate was determined.

Investigation of the unfolding behaviour of CCld revealed a continuous rise of fluorescence at 350 nm, representing the denaturation process, with an intermediate step at a concentration of 2.5 M GdnHCl. Absorbance at 407 nm was completely lost at a concentration of about 2.5 M GdnHCl in a two-state transition. Comparison of unfolding parameters suggested that during the unfolding process native CCld is followed by a heme-bound intermediate, which is followed by a heme-free denatured state. ΔG_{H_2O} of CCld was calculated to be 4.3 kJ*mol^{-1} which is 4 times lower compared to NdCld with a value of 16.3 kJ*mol^{-1} [40], indicating a lower conformational stability. The heme cavities of CCld and NdCld exhibit a similar stability with both sharing the value of 12.7 kJ*mol^{-1} which is unexpected since NwCld shows a lower stability with respect to NdCld [40] while sharing a similar distal and proximal heme architecture with CCld [13].

When titrated with different ligands, dissociation constants of CCld were similar in comparison to NdCld while the differences between pH 7.0 and pH 5.5 were less pronounced in CCld compared to NdCld.

Fluoride acted as a high-spin ligand. When titrated with either nitrite or thiocyanate, CT1 disappeared which reflects the spectral behaviour of CCld in the presence of a low-spin ligand.

Structural studies revealed the dimeric assembly of crystallized CCld in complex with imidazole and thiocyanate. Moreover, the architecture of the heme cavity including heme planarity and the behaviour of some of the active site residues was investigated. Binding of a ligand did not lead to a notable change in distal and proximal architecture. As it turned out, native CCld was contaminated with imidazole, rendering a comparison of a native state with CCld in complex with thiocyanate impossible. All structures showed a similar heme architecture. Interestingly, both, CCld in complex with imidazole and thiocyanate, showed a visible tilt in their porphyrin rings while the true reason for this phenomenon keeps unexplained. Moreover, one molecule of MPD was found in both structures in a small cavity on the surface of the protein. The oxygens of the nearby R128 likely mediate weak electrostatic interactions with it to keep it in place. Lastly, it was not possible to assign the occupation of a very prominent area of positive electron density which is present in all structures near R4. It is believed to be the negatively charged ion chloride, but adding it to the model did not change the positive electron density, probably because its anomalous signal is not high enough.

6 Supplementary Figures

CrystalTrak Reservoir Design Grid Report for User 'Djinovic'

Screen Name: ccld intial

target pH value in (), .. indicates truncated chemical name

	1	2	3	4	5	6	7	8	9	10	11	12
A	PEG 3350 16 w/v AmCl 0.2 M	PEG 335..16.82 w/v AmCl 0.2 M	PEG 335..17.64 w/v AmCl 0.2 M	PEG 335..18.45 w/v AmCl 0.2 M	PEG 335..19.27 w/v AmCl 0.2 M	PEG 335..20.09 w/v AmCl 0.2 M	PEG 335..20.91 w/v AmCl 0.2 M	PEG 335..21.73 w/v AmCl 0.2 M	PEG 335..22.55 w/v AmCl 0.2 M	PEG 335..23.36 w/v AmCl 0.2 M	PEG 335..24.18 w/v AmCl 0.2 M	PEG 3350 25 w/v AmCl 0.2 M
B	PEG 3350 16 w/v AmCl 0.2 M Glyerol 5 w/v	PEG 335..16.82 w/v AmCl 0.2 M Glyerol 5 w/v	PEG 335..17.64 w/v AmCl 0.2 M Glyerol 5 w/v	PEG 335..18.45 w/v AmCl 0.2 M Glyerol 5 w/v	PEG 335..19.27 w/v AmCl 0.2 M Glyerol 5 w/v	PEG 335..20.09 w/v AmCl 0.2 M Glyerol 5 w/v	PEG 335..20.91 w/v AmCl 0.2 M Glyerol 5 w/v	PEG 335..21.73 w/v AmCl 0.2 M Glyerol 5 w/v	PEG 335..22.55 w/v AmCl 0.2 M Glyerol 5 w/v	PEG 335..23.36 w/v AmCl 0.2 M Glyerol 5 w/v	PEG 335..24.18 w/v AmCl 0.2 M Glyerol 5 w/v	PEG 3350 25 w/v AmCl 0.2 M Glyerol 5 w/v
C	PEG 3350 16 w/v nacl 0.2 M bis-tris 0.1 M (5.5)	PEG 335..16.82 w/v nacl 0.2 M bis-tris 0.1 M (5.5)	PEG 335..17.64 w/v nacl 0.2 M bis-tris 0.1 M (5.5)	PEG 335..18.45 w/v nacl 0.2 M bis-tris 0.1 M (5.5)	PEG 335..19.27 w/v nacl 0.2 M bis-tris 0.1 M (5.5)	PEG 335..20.09 w/v nacl 0.2 M bis-tris 0.1 M (5.5)	PEG 335..20.91 w/v nacl 0.2 M bis-tris 0.1 M (5.5)	PEG 335..21.73 w/v nacl 0.2 M bis-tris 0.1 M (5.5)	PEG 335..22.55 w/v nacl 0.2 M bis-tris 0.1 M (5.5)	PEG 335..23.36 w/v nacl 0.2 M bis-tris 0.1 M (5.5)	PEG 335..24.18 w/v nacl 0.2 M bis-tris 0.1 M (5.5)	PEG 3350 25 w/v nacl 0.2 M bis-tris 0.1 M (5.5)
D	PEG 3350 16 w/v nacl 0.2 M bis-tris 0.1 M (6)	PEG 335..16.82 w/v nacl 0.2 M bis-tris 0.1 M (6)	PEG 335..17.64 w/v nacl 0.2 M bis-tris 0.1 M (6)	PEG 335..18.45 w/v nacl 0.2 M bis-tris 0.1 M (6)	PEG 335..19.27 w/v nacl 0.2 M bis-tris 0.1 M (6)	PEG 335..20.09 w/v nacl 0.2 M bis-tris 0.1 M (6)	PEG 335..20.91 w/v nacl 0.2 M bis-tris 0.1 M (6)	PEG 335..21.73 w/v nacl 0.2 M bis-tris 0.1 M (6)	PEG 335..22.55 w/v nacl 0.2 M bis-tris 0.1 M (6)	PEG 335..23.36 w/v nacl 0.2 M bis-tris 0.1 M (6)	PEG 335..24.18 w/v nacl 0.2 M bis-tris 0.1 M (6)	PEG 3350 25 w/v nacl 0.2 M bis-tris 0.1 M (6)
E	PEG 3350 16 w/v nacl 0.2 M bis-tris 0.1 M (6.5)	PEG 335..16.82 w/v nacl 0.2 M bis-tris 0.1 M (6.5)	PEG 335..17.64 w/v nacl 0.2 M bis-tris 0.1 M (6.5)	PEG 335..18.45 w/v nacl 0.2 M bis-tris 0.1 M (6.5)	PEG 335..19.27 w/v nacl 0.2 M bis-tris 0.1 M (6.5)	PEG 335..20.09 w/v nacl 0.2 M bis-tris 0.1 M (6.5)	PEG 335..20.91 w/v nacl 0.2 M bis-tris 0.1 M (6.5)	PEG 335..21.73 w/v nacl 0.2 M bis-tris 0.1 M (6.5)	PEG 335..22.55 w/v nacl 0.2 M bis-tris 0.1 M (6.5)	PEG 335..23.36 w/v nacl 0.2 M bis-tris 0.1 M (6.5)	PEG 335..24.18 w/v nacl 0.2 M bis-tris 0.1 M (6.5)	PEG 3350 25 w/v nacl 0.2 M bis-tris 0.1 M (6.5)
F	PEG 3350 16 w/v nacl 0.2 M bis-tris 0.1 M (7)	PEG 335..16.82 w/v nacl 0.2 M bis-tris 0.1 M (7)	PEG 335..17.64 w/v nacl 0.2 M bis-tris 0.1 M (7)	PEG 335..18.45 w/v nacl 0.2 M bis-tris 0.1 M (7)	PEG 335..19.27 w/v nacl 0.2 M bis-tris 0.1 M (7)	PEG 335..20.09 w/v nacl 0.2 M bis-tris 0.1 M (7)	PEG 335..20.91 w/v nacl 0.2 M bis-tris 0.1 M (7)	PEG 335..21.73 w/v nacl 0.2 M bis-tris 0.1 M (7)	PEG 335..22.55 w/v nacl 0.2 M bis-tris 0.1 M (7)	PEG 335..23.36 w/v nacl 0.2 M bis-tris 0.1 M (7)	PEG 335..24.18 w/v nacl 0.2 M bis-tris 0.1 M (7)	PEG 3350 25 w/v nacl 0.2 M bis-tris 0.1 M (7)
G	Glyerol 5 w/v bis-tris 0.1 M (6.5) PEG 3350 16 w/v nacl 0.2 M	Glyerol 5 w/v bis-tris 0.1 M (6.5) PEG 335..16.82 w/v nacl 0.2 M	Glyerol 5 w/v bis-tris 0.1 M (6.5) PEG 335..17.64 w/v nacl 0.2 M	Glyerol 5 w/v bis-tris 0.1 M (6.5) PEG 335..18.45 w/v nacl 0.2 M	Glyerol 5 w/v bis-tris 0.1 M (6.5) PEG 335..19.27 w/v nacl 0.2 M	Glyerol 5 w/v bis-tris 0.1 M (6.5) PEG 335..20.09 w/v nacl 0.2 M	Glyerol 5 w/v bis-tris 0.1 M (6.5) PEG 335..20.91 w/v nacl 0.2 M	Glyerol 5 w/v bis-tris 0.1 M (6.5) PEG 335..21.73 w/v nacl 0.2 M	Glyerol 5 w/v bis-tris 0.1 M (6.5) PEG 335..22.55 w/v nacl 0.2 M	Glyerol 5 w/v bis-tris 0.1 M (6.5) PEG 335..23.36 w/v nacl 0.2 M	Glyerol 5 w/v bis-tris 0.1 M (6.5) PEG 335..24.18 w/v nacl 0.2 M	Glyerol 5 w/v bis-tris 0.1 M (6.5) PEG 3350 25 w/v nacl 0.2 M
H	MES 0.1 M (6.5) mgso4 1.2 M	MES 0.1 M (6.5) mgso4 1.25 M	MES 0.1 M (6.5) mgso4 1.31 M	MES 0.1 M (6.5) mgso4 1.36 M	MES 0.1 M (6.5) mgso4 1.42 M	MES 0.1 M (6.5) mgso4 1.47 M	MES 0.1 M (6.5) mgso4 1.53 M	MES 0.1 M (6.5) mgso4 1.58 M	MES 0.1 M (6.5) mgso4 1.64 M	MES 0.1 M (6.5) mgso4 1.69 M	MES 0.1 M (6.5) mgso4 1.75 M	MES 0.1 M (6.5) mgso4 1.8 M

11/6/2014 2:51:14 PM

Supplementary Figure 6.1: Init Screen.

CrystalTrak Reservoir Design Grid Report for User 'Djinovic'

Screen Name: ccld opt2 MgSO4 NaCl

target pH value in (), .. indicates truncated chemical name

	1	2	3	4	5	6	7	8	9	10	11	12
A	mgso4 1.2 M MES 0.1 M (6)	mgso4 1.25 M MES 0.1 M (6)	mgso4 1.31 M MES 0.1 M (6)	mgso4 1.36 M MES 0.1 M (6)	mgso4 1.42 M MES 0.1 M (6)	mgso4 1.47 M MES 0.1 M (6)	mgso4 1.53 M MES 0.1 M (6)	mgso4 1.58 M MES 0.1 M (6)	mgso4 1.64 M MES 0.1 M (6)	mgso4 1.69 M MES 0.1 M (6)	mgso4 1.75 M MES 0.1 M (6)	mgso4 1.8 M MES 0.1 M (6)
B	mgso4 1.2 M MES 0.1 M (6.5)	mgso4 1.25 M MES 0.1 M (6.5)	mgso4 1.31 M MES 0.1 M (6.5)	mgso4 1.36 M MES 0.1 M (6.5)	mgso4 1.42 M MES 0.1 M (6.5)	mgso4 1.47 M MES 0.1 M (6.5)	mgso4 1.53 M MES 0.1 M (6.5)	mgso4 1.58 M MES 0.1 M (6.5)	mgso4 1.64 M MES 0.1 M (6.5)	mgso4 1.69 M MES 0.1 M (6.5)	mgso4 1.75 M MES 0.1 M (6.5)	mgso4 1.8 M MES 0.1 M (6.5)
C	mgso4 1.2 M MES 0.1 M (7)	mgso4 1.25 M MES 0.1 M (7)	mgso4 1.31 M MES 0.1 M (7)	mgso4 1.36 M MES 0.1 M (7)	mgso4 1.42 M MES 0.1 M (7)	mgso4 1.47 M MES 0.1 M (7)	mgso4 1.53 M MES 0.1 M (7)	mgso4 1.58 M MES 0.1 M (7)	mgso4 1.64 M MES 0.1 M (7)	mgso4 1.69 M MES 0.1 M (7)	mgso4 1.75 M MES 0.1 M (7)	mgso4 1.8 M MES 0.1 M (7)
D	mgso4 0.05 M MES 0.1 M (6.5) PEG 3350 22 w/v	mgso4 0.09 M MES 0.1 M (6.5) PEG 3350 22 w/v	mgso4 0.13 M MES 0.1 M (6.5) PEG 3350 22 w/v	mgso4 0.17 M MES 0.1 M (6.5) PEG 3350 22 w/v	mgso4 0.21 M MES 0.1 M (6.5) PEG 3350 22 w/v	mgso4 0.25 M MES 0.1 M (6.5) PEG 3350 22 w/v	mgso4 0.3 M MES 0.1 M (6.5) PEG 3350 22 w/v	mgso4 0.34 M MES 0.1 M (6.5) PEG 3350 22 w/v	mgso4 0.38 M MES 0.1 M (6.5) PEG 3350 22 w/v	mgso4 0.42 M MES 0.1 M (6.5) PEG 3350 22 w/v	mgso4 0.46 M MES 0.1 M (6.5) PEG 3350 22 w/v	mgso4 0.5 M MES 0.1 M (6.5) PEG 3350 22 w/v
E	mgso4 0.05 M MES 0.1 M (6.5) MPD 25 v/v	mgso4 0.09 M MES 0.1 M (6.5) MPD 25 v/v	mgso4 0.13 M MES 0.1 M (6.5) MPD 25 v/v	mgso4 0.17 M MES 0.1 M (6.5) MPD 25 v/v	mgso4 0.21 M MES 0.1 M (6.5) MPD 25 v/v	mgso4 0.25 M MES 0.1 M (6.5) MPD 25 v/v	mgso4 0.3 M MES 0.1 M (6.5) MPD 25 v/v	mgso4 0.34 M MES 0.1 M (6.5) MPD 25 v/v	mgso4 0.38 M MES 0.1 M (6.5) MPD 25 v/v	mgso4 0.42 M MES 0.1 M (6.5) MPD 25 v/v	mgso4 0.46 M MES 0.1 M (6.5) MPD 25 v/v	mgso4 0.5 M MES 0.1 M (6.5) MPD 25 v/v
F	MES 0.1 M (6.5) Glyerol 5 v/v mgso4 1.2 M	MES 0.1 M (6.5) Glyerol 5 v/v mgso4 1.23 M	MES 0.1 M (6.5) Glyerol 5 v/v mgso4 1.25 M	MES 0.1 M (6.5) Glyerol 5 v/v mgso4 1.28 M	MES 0.1 M (6.5) Glyerol 5 v/v mgso4 1.31 M	MES 0.1 M (6.5) Glyerol 5 v/v mgso4 1.34 M	MES 0.1 M (6.5) Glyerol 5 v/v mgso4 1.36 M	MES 0.1 M (6.5) Glyerol 5 v/v mgso4 1.39 M	MES 0.1 M (6.5) Glyerol 5 v/v mgso4 1.42 M	MES 0.1 M (6.5) Glyerol 5 v/v mgso4 1.45 M	MES 0.1 M (6.5) Glyerol 5 v/v mgso4 1.47 M	MES 0.1 M (6.5) Glyerol 5 v/v mgso4 1.5 M
G	nacl 0.1 M MES 0.1 M (6.5)	nacl 0.18 M MES 0.1 M (6.5)	nacl 0.26 M MES 0.1 M (6.5)	nacl 0.35 M MES 0.1 M (6.5)	nacl 0.43 M MES 0.1 M (6.5)	nacl 0.51 M MES 0.1 M (6.5)	nacl 0.59 M MES 0.1 M (6.5)	nacl 0.67 M MES 0.1 M (6.5)	nacl 0.75 M MES 0.1 M (6.5)	nacl 0.84 M MES 0.1 M (6.5)	nacl 0.92 M MES 0.1 M (6.5)	nacl 1 M MES 0.1 M (6.5)
H	nacl 0.1 M bis-tris 0.1 M (6.5) PEG 3350 22 w/v	nacl 0.18 M bis-tris 0.1 M (6.5) PEG 3350 22 w/v	nacl 0.26 M bis-tris 0.1 M (6.5) PEG 3350 22 w/v	nacl 0.35 M bis-tris 0.1 M (6.5) PEG 3350 22 w/v	nacl 0.43 M bis-tris 0.1 M (6.5) PEG 3350 22 w/v	nacl 0.51 M bis-tris 0.1 M (6.5) PEG 3350 22 w/v	nacl 0.59 M bis-tris 0.1 M (6.5) PEG 3350 22 w/v	nacl 0.67 M bis-tris 0.1 M (6.5) PEG 3350 22 w/v	nacl 0.75 M bis-tris 0.1 M (6.5) PEG 3350 22 w/v	nacl 0.84 M bis-tris 0.1 M (6.5) PEG 3350 22 w/v	nacl 0.92 M bis-tris 0.1 M (6.5) PEG 3350 22 w/v	nacl 1 M bis-tris 0.1 M (6.5) PEG 3350 22 w/v

11/4/2014 2:02:22 PM

Supplementary Figure 6.2: Opt2 Screen.

CrystalTrak Reservoir Design Grid Report for User 'Supervisor'

Screen Name: ccld opt3 mgso4 peg mes bistris

target pH value in (), .. indicates truncated chemical name

	1	2	3	4	5	6	7	8	9	10	11	12
A	PEG 3350 22 w/v MES 0.1 M (6)	mgso4 0.04 M PEG 3350 22 w/v MES 0.1 M (6)	mgso4 0.07 M PEG 3350 22 w/v MES 0.1 M (6)	mgso4 0.11 M PEG 3350 22 w/v MES 0.1 M (6)	mgso4 0.15 M PEG 3350 22 w/v MES 0.1 M (6)	mgso4 0.18 M PEG 3350 22 w/v MES 0.1 M (6)	mgso4 0.22 M PEG 3350 22 w/v MES 0.1 M (6)	mgso4 0.25 M PEG 3350 22 w/v MES 0.1 M (6)	mgso4 0.29 M PEG 3350 22 w/v MES 0.1 M (6)	mgso4 0.33 M PEG 3350 22 w/v MES 0.1 M (6)	mgso4 0.36 M PEG 3350 22 w/v MES 0.1 M (6)	mgso4 0.4 M PEG 3350 22 w/v MES 0.1 M (6)
B	PEG 3350 22 w/v MES 0.1 M (6.5)	mgso4 0.04 M PEG 3350 22 w/v MES 0.1 M (6.5)	mgso4 0.07 M PEG 3350 22 w/v MES 0.1 M (6.5)	mgso4 0.11 M PEG 3350 22 w/v MES 0.1 M (6.5)	mgso4 0.15 M PEG 3350 22 w/v MES 0.1 M (6.5)	mgso4 0.18 M PEG 3350 22 w/v MES 0.1 M (6.5)	mgso4 0.22 M PEG 3350 22 w/v MES 0.1 M (6.5)	mgso4 0.25 M PEG 3350 22 w/v MES 0.1 M (6.5)	mgso4 0.29 M PEG 3350 22 w/v MES 0.1 M (6.5)	mgso4 0.33 M PEG 3350 22 w/v MES 0.1 M (6.5)	mgso4 0.36 M PEG 3350 22 w/v MES 0.1 M (6.5)	mgso4 0.4 M PEG 3350 22 w/v MES 0.1 M (6.5)
C	PEG 3350 22 w/v MES 0.1 M (7)	mgso4 0.04 M PEG 3350 22 w/v MES 0.1 M (7)	mgso4 0.07 M PEG 3350 22 w/v MES 0.1 M (7)	mgso4 0.11 M PEG 3350 22 w/v MES 0.1 M (7)	mgso4 0.15 M PEG 3350 22 w/v MES 0.1 M (7)	mgso4 0.18 M PEG 3350 22 w/v MES 0.1 M (7)	mgso4 0.22 M PEG 3350 22 w/v MES 0.1 M (7)	mgso4 0.25 M PEG 3350 22 w/v MES 0.1 M (7)	mgso4 0.29 M PEG 3350 22 w/v MES 0.1 M (7)	mgso4 0.33 M PEG 3350 22 w/v MES 0.1 M (7)	mgso4 0.36 M PEG 3350 22 w/v MES 0.1 M (7)	mgso4 0.4 M PEG 3350 22 w/v MES 0.1 M (7)
D	PEG 3350 22 w/v Glyerol 5 v/v MES 0.1 M (6.5)	mgso4 0.04 M PEG 3350 22 w/v Glyerol 5 v/v MES 0.1 M (6.5)	mgso4 0.07 M PEG 3350 22 w/v Glyerol 5 v/v MES 0.1 M (6.5)	mgso4 0.11 M PEG 3350 22 w/v Glyerol 5 v/v MES 0.1 M (6.5)	mgso4 0.15 M PEG 3350 22 w/v Glyerol 5 v/v MES 0.1 M (6.5)	mgso4 0.18 M PEG 3350 22 w/v Glyerol 5 v/v MES 0.1 M (6.5)	mgso4 0.22 M PEG 3350 22 w/v Glyerol 5 v/v MES 0.1 M (6.5)	mgso4 0.25 M PEG 3350 22 w/v Glyerol 5 v/v MES 0.1 M (6.5)	mgso4 0.29 M PEG 3350 22 w/v Glyerol 5 v/v MES 0.1 M (6.5)	mgso4 0.33 M PEG 3350 22 w/v Glyerol 5 v/v MES 0.1 M (6.5)	mgso4 0.36 M PEG 3350 22 w/v Glyerol 5 v/v MES 0.1 M (6.5)	mgso4 0.4 M PEG 3350 22 w/v Glyerol 5 v/v MES 0.1 M (6.5)
E	mgso4 1.2 M MES 0.1 M (6.5)	mgso4 1.25 M MES 0.1 M (6.5)	mgso4 1.31 M MES 0.1 M (6.5)	mgso4 1.36 M MES 0.1 M (6.5)	mgso4 1.42 M MES 0.1 M (6.5)	mgso4 1.47 M MES 0.1 M (6.5)	mgso4 1.53 M MES 0.1 M (6.5)	mgso4 1.58 M MES 0.1 M (6.5)	mgso4 1.64 M MES 0.1 M (6.5)	mgso4 1.69 M MES 0.1 M (6.5)	mgso4 1.75 M MES 0.1 M (6.5)	mgso4 1.8 M MES 0.1 M (6.5)
F	mgso4 1.2 M Glyerol 5 v/v MES 0.1 M (6.5)	mgso4 1.25 M Glyerol 5 v/v MES 0.1 M (6.5)	mgso4 1.31 M Glyerol 5 v/v MES 0.1 M (6.5)	mgso4 1.36 M Glyerol 5 v/v MES 0.1 M (6.5)	mgso4 1.42 M Glyerol 5 v/v MES 0.1 M (6.5)	mgso4 1.47 M Glyerol 5 v/v MES 0.1 M (6.5)	mgso4 1.53 M Glyerol 5 v/v MES 0.1 M (6.5)	mgso4 1.58 M Glyerol 5 v/v MES 0.1 M (6.5)	mgso4 1.64 M Glyerol 5 v/v MES 0.1 M (6.5)	mgso4 1.69 M Glyerol 5 v/v MES 0.1 M (6.5)	mgso4 1.75 M Glyerol 5 v/v MES 0.1 M (6.5)	mgso4 1.8 M Glyerol 5 v/v MES 0.1 M (6.5)
G	PEG 3350 22 w/v MES 0.1 M (6.5)	nacl 0.07 M PEG 3350 22 w/v MES 0.1 M (6.5)	nacl 0.15 M PEG 3350 22 w/v MES 0.1 M (6.5)	nacl 0.22 M PEG 3350 22 w/v MES 0.1 M (6.5)	nacl 0.29 M PEG 3350 22 w/v MES 0.1 M (6.5)	nacl 0.36 M PEG 3350 22 w/v MES 0.1 M (6.5)	nacl 0.44 M PEG 3350 22 w/v MES 0.1 M (6.5)	nacl 0.51 M PEG 3350 22 w/v MES 0.1 M (6.5)	nacl 0.58 M PEG 3350 22 w/v MES 0.1 M (6.5)	nacl 0.65 M PEG 3350 22 w/v MES 0.1 M (6.5)	nacl 0.73 M PEG 3350 22 w/v MES 0.1 M (6.5)	nacl 0.8 M PEG 3350 22 w/v MES 0.1 M (6.5)
H	PEG 3350 22 w/v Glyerol 5 v/v bis-tris 0.1 M (6.5)	nacl 0.07 M PEG 3350 22 w/v Glyerol 5 v/v bis-tris 0.1 M (6.5)	nacl 0.15 M PEG 3350 22 w/v Glyerol 5 v/v bis-tris 0.1 M (6.5)	nacl 0.22 M PEG 3350 22 w/v Glyerol 5 v/v bis-tris 0.1 M (6.5)	nacl 0.29 M PEG 3350 22 w/v Glyerol 5 v/v bis-tris 0.1 M (6.5)	nacl 0.36 M PEG 3350 22 w/v Glyerol 5 v/v bis-tris 0.1 M (6.5)	nacl 0.44 M PEG 3350 22 w/v Glyerol 5 v/v bis-tris 0.1 M (6.5)	nacl 0.51 M PEG 3350 22 w/v Glyerol 5 v/v bis-tris 0.1 M (6.5)	nacl 0.58 M PEG 3350 22 w/v Glyerol 5 v/v bis-tris 0.1 M (6.5)	nacl 0.65 M PEG 3350 22 w/v Glyerol 5 v/v bis-tris 0.1 M (6.5)	nacl 0.73 M PEG 3350 22 w/v Glyerol 5 v/v bis-tris 0.1 M (6.5)	nacl 0.8 M PEG 3350 22 w/v Glyerol 5 v/v bis-tris 0.1 M (6.5)

11/4/2014 2:57:57 PM

Supplementary Figure 6.3: Opt3 Screen.

7 Bibliography

1. Van Ginkel CG, Rikken GB, Kroon AGM, Kengen SWM. Purification and characterization of chlorite dismutase: A novel oxygen-generating enzyme. *Arch Microbiol*. 1996;166(5):321-326. doi:10.1007/s002030050390.

2. Rikken GB, Kroon AGM, Van Ginkel CG. Transformation of (per)chlorate into chloride by a newly isolated bacterium: Reduction and dismutation. *Appl Microbiol Biotechnol*. 1996;45(3):420-426. doi:10.1007/s002530050707.

3. Ettwig KF, Butler MK, Le Paslier D, et al. Nitrite-driven anaerobic methane oxidation by oxygenic bacteria. *Nature*. 2010;464(7288):543-548. doi:10.1038/nature08883.

4. Coates JD, Achenbach L a. Microbial perchlorate reduction: rocket-fueled metabolism. *Nat Rev Microbiol*. 2004;2(7):569-580. doi:10.1038/nrmicro926.

5. Hofbauer S, Schaffner I, Furtmüller PG, Obinger C. Chlorite dismutases - a heme enzyme family for use in bioremediation and generation of molecular oxygen. *Biotechnol J*. 2014;9(4):461-473. doi:10.1002/biot.201300210.

6. Schaffner I, Hofbauer S, Krutzler M, et al. Dimeric chlorite dismutase from the nitrogen-fixing cyanobacterium Cyanothece sp. PCC7425. *Mol Microbiol*. 2015;96(5):1053-1068. doi:10.1111/mmi.12989.

7. Fischer J, Holliday G, Thornton J. The CoFactor database: organic cofactors in enzyme catalysis. http://www.ebi.ac.uk. Accessed July 11, 2017.

8. Kostan J, Sjöblom B, Maixner F, et al. Structural and functional characterisation of the chlorite dismutase from the nitrite-oxidizing bacterium " Candidatus Nitrospira defluvii": Identification of a catalytically important amino acid residue. *J Struct Biol*. 2010;172(3):331-342. doi:10.1016/j.jsb.2010.06.014.

9. Hofbauer S, Gysel K, Bellei M, et al. Manipulating conserved heme cavity residues of chlorite dismutase: Effect on structure, redox chemistry, and reactivity. *Biochemistry*. 2014;53(1):77-89. doi:10.1021/bi401042z.

10. Hofbauer S, Howes BD, Flego N, et al. From chlorite dismutase towards HemQ-the role of the proximal H-bonding network in haeme binding. *Biosci Rep*. 2016;36(2):e00312. doi:10.1042/BSR20150330.

11. Hofbauer S, Hagmüller A, Schaffner I, et al. Structure and heme-binding properties of HemQ (chlorite dismutase-like protein) from Listeria monocytogenes. *Arch Biochem Biophys*. 2015;574:36-48. doi:10.1016/j.abb.2015.01.010.

12. Hofbauer S, Mlynek G, Milazzo L, et al. Hydrogen peroxide-mediated conversion of coproheme to heme b by HemQ—lessons from the first crystal structure and kinetic studies. *FEBS J*. 2016;283(23):4386-4401. doi:10.1111/febs.13930.

13. Mlynek G, Sjöblom B, Kostan J, et al. Unexpected diversity of chlorite dismutases: A catalytically efficient dimeric enzyme from Nitrobacter winogradskyi. *J Bacteriol*. 2011;193(10):2408-2417. doi:10.1128/JB.01262-10.

14. Celis AI, Geeraerts Z, Ngmenterebo D, et al. A dimeric chlorite dismutase exhibits O2-generating activity and acts as a chlorite antioxidant in Klebsiella pneumoniae MGH 78578. *Biochemistry*.

2015;54(2):434-446. doi:10.1021/bi501184c.

15. Lee AQ, Streit BR, Zdilla MJ, Abu-Omar MM, DuBois JL. Mechanism of and exquisite selectivity for O-O bond formation by the heme-dependent chlorite dismutase. *Proc Natl Acad Sci U S A*. 2008;105(41):15654-15659. doi:10.1073/pnas.0804279105.

16. Keith JM, Abu-Omar MM, Hall MB. Computational investigation of the concerted dismutation of chlorite ion by water-soluble iron porphyrins. *Inorg Chem*. 2011;50(17):7928-7930. doi:10.1021/ic2009732.

17. Sun S, Li Z-S, Chen S-L. A Dominant Homolytic O-Cl Bond Cleavage with Low-Spin Triplet-State Fe(IV)=O Formed is Revealed in the Mechanism of Heme-Dependent Chlorite Dismutase. *Dalt Trans*. 2014;43(3):973-981. doi:10.1039/c3dt52171k.

18. Hofbauer S, Gruber C, Pirker KF, et al. Transiently produced hypochlorite is responsible for the irreversible inhibition of chlorite dismutase. *Biochemistry*. 2014;53(19):3145-3157. doi:10.1021/bi500401k.

19. Lambert JB, Gronert S, Shurvell HF, Lightner DA. *Spektroskopie - Strukturaufklärung in Der Organischen Chemie*. Second. Pearson Studium; 2012.

20. Furtmüller P. *Biochemical Practical Course II (772305)*. Vienna; 2013.

21. Böhm G, Muhr R, Jaenicke R. Quantitative analysis of protein far UV circular dichroism spectra by neural networks. *Protein Eng*. 1992;5(3):191-195. doi:10.1093/protein/5.3.191.

22. Djinovic-Carugo K. *Macromolecular Crystallography*. Vienna; 2014.

23. Wlodawer A, Minor W, Dauter Z, Jaskolski M. Protein crystallography for aspiring crystallographers or how to avoid pitfalls and traps in macromolecular structure determination. *FEBS J*. 2013;280(22):5705-5736. doi:10.1111/febs.12495.

24. Murshudov GN, Skubák P, Lebedev AA, et al. REFMAC5 for the refinement of macromolecular crystal structures. *Acta Crystallogr Sect D Biol Crystallogr*. 2011;67(4):355-367. doi:10.1107/S0907444911001314.

25. Adams PD, Afonine P V., Bunkóczi G, et al. PHENIX: A comprehensive Python-based system for macromolecular structure solution. *Acta Crystallogr Sect D Biol Crystallogr*. 2010;66(2):213-221. doi:10.1107/S0907444909052925.

26. Gabadinho J, Beteva A, Guijarro M, et al. MxCuBE: A synchrotron beamline control environment customized for macromolecular crystallography experiments. *J Synchrotron Radiat*. 2010;17(5):700-707. doi:10.1107/S0909049510020005.

27. Merrit E. X-ray Anomalous Scattering. doi:http://skuld.bmsc.washington.edu/scatter/AS_index.html.

28. Brennan S, Cowan PL. A suite of programs for calculating x-ray absorption, reflection, and diffraction performance for a variety of materials at arbitrary wavelengths. *Rev Sci Instrum*. 1992;63(1):850-853. doi:10.1063/1.1142625.

29. Kabsch W. Integration, scaling, space-group assignment and post-refinement. *Acta Crystallogr Sect D Biol Crystallogr*. 2010;66(2):133-144. doi:10.1107/S0907444909047374.

30. Kabsch W. XDS. *Acta Crystallogr Sect D Biol Crystallogr*. 2010;66(2):125-132.

doi:10.1107/S0907444909047337.

31. Long F, Vagin AA, Young P, Murshudov GN. BALBES: A molecular-replacement pipeline. *Acta Crystallogr Sect D Biol Crystallogr*. 2007;64(1):125-132. doi:10.1107/S0907444907050172.

32. Terwilliger TC, Adams PD, Read RJ, et al. Decision-making in structure solution using Bayesian estimates of map quality: The PHENIX AutoSol wizard. *Acta Crystallogr Sect D Biol Crystallogr*. 2009;65(6):582-601. doi:10.1107/S0907444909012098.

33. Painter J, Merritt EA. Optimal description of a protein structure in terms of multiple groups undergoing TLS motion. *Acta Crystallogr Sect D Biol Crystallogr*. 2006;62(4):439-450. doi:10.1107/S0907444906005270.

34. Emsley P, Cowtan K. Coot: Model-building tools for molecular graphics. *Acta Crystallogr Sect D Biol Crystallogr*. 2004;60(12 I):2126-2132. doi:10.1107/S0907444904019158.

35. Emsley P, Lohkamp B, Scott WG, Cowtan K. Features and development of Coot. *Acta Crystallogr Sect D Biol Crystallogr*. 2010;66(4):486-501. doi:10.1107/S0907444910007493.

36. Davis IW, Leaver-Fay A, Chen VB, et al. MolProbity: All-atom contacts and structure validation for proteins and nucleic acids. *Nucleic Acids Res*. 2007;35(SUPPL.2):375-383. doi:10.1093/nar/gkm216.

37. Chen VB, Arendall WB, Headd JJ, et al. MolProbity: All-atom structure validation for macromolecular crystallography. *Acta Crystallogr Sect D Biol Crystallogr*. 2010;66(1):12-21. doi:10.1107/S0907444909042073.

38. Joosten RP, Long F, Murshudov GN, Perrakis A. The {\it PDB_REDO} server for macromolecular structure model optimization. *IUCrJ*. 2014;1:213-220. doi:10.1107/S2052252514009324.

39. Kelly SM, Jess TJ, Price NC. How to study proteins by circular dichroism. *Biochim Biophys Acta - Proteins Proteomics*. 2005;1751(2):119-139. doi:10.1016/j.bbapap.2005.06.005.

40. Hofbauer S, Gysel K, Mlynek G, et al. Impact of subunit and oligomeric structure on the thermal and conformational stability of chlorite dismutases. *Biochim Biophys Acta - Proteins Proteomics*. 2012;1824(9):1031-1038. doi:10.1016/j.bbapap.2012.05.012.

41. Howes BD, Feis A, Indiani C, Marzocchi MP, Smulevich G. Formation of two types of low-spin heme in horseradish peroxidase isoenzyme A2 at low temperature. *J Biol Inorg Chem*. 2000;5(2):227-235.

42. Schrodinger LLC. The PyMOL Molecular Graphics System, Version 1.8. 2015.

43. Kabesova, M.;Gazo J. Structure and classification of thiocyanates and the mutual influence of their ligands. *Chem Rev*. 1980;34(6):41.

44. de Geus DC, Thomassen EAJ, Hagedoorn PL, Pannu NS, van Duijn E, Abrahams JP. Crystal Structure of Chlorite Dismutase, a Detoxifying Enzyme Producing Molecular Oxygen. *J Mol Biol*. 2009;387(1):192-206. doi:10.1016/j.jmb.2009.01.036.

45. Cromer DT, Liberman D. Relativistic Calculation of Anomalous Scattering Factors for X Rays. *J Chem Phys*. 1970;53(5):1891-1898. doi:doi:10.1063/1.1674266.

Index

LB-Amp	Lysogeny broth medium supplemented with 100 µg/ml ampicillin
CCld	Chlorite dismutase from *Cyanothece* sp. PCC7425
CIP	Cleaning in place
Cld	Chlorite dismutase
CV	Column volumes
CT band	Charge-transfer band
DyP	Dye-decolorizing peroxidase
eCD	Electronic circular dichroism
EDTA	Ethylenediaminetetraacetic acid
ESRF	European Synchrotron Radiation Facility
GdnHCl	Guanidine hydrochloride
HQ-H_2O	High quality water
IPTG	Isopropyl β-D-1-thiogalactopyranoside
LmCld	Chlorite dismutase from *Listeria monocytogenes*
MES	2-(N-morpholino)ethanesulfonic
MPD	2-Methyl-2,4-pentanediol
MR	Molecular replacement
NdCld	Chlorite dismutase from "*Candidatus* Nitrospira defluvii"
NMR	Nuclear magnetic resonance
NwCld	Chlorite dismutase of *Nitrobacter windogradskyi*
PCRB	Perchlorate reducing bacteria
PDB	Protein databank
PEM	Photoelastic modulator
PMSF	Phenylmethanesulfonylfluoride
R_Z	Reinheitszahl
SAD	Single wavelength anomalous dispersion
SEC	Size exclusion chromatography